Universidade de Aveiro Departamento de Engenharia Mecânica

2020

Eduarda Manuela Marantes Pereira da Silva

Development of an experiment plan with an Electrospinning equipment for cartilage Tissue Engineering

Desenvolvimento de plano de experiências com equipamento de eletrofiação para Engenharia de Tecidos de cartilagem

Universidade de Aveiro Departamento de Engenharia Mecânica

2020

Eduarda Manuela Marantes Pereira da Silva

Development of an experiment plan with an Electrospinning equipment for cartilage Tissue Engineering

Desenvolvimento de plano de experiências com equipamento de eletrofiação para Engenharia de Tecidos de cartilagem

Dissertação apresentada à Universidade de Aveiro para cumprimento dos requisitos necessários à obtenção do grau de Mestre em Engenharia Mecânica, realizada sob orientação científica do António Manuel Godinho Completo, Professor Associado com Agregação do Departamento de Engenharia Mecânica da Universidade de Aveiro e da Doutora Paula Alexandrina de Aguiar Pereira Marques, equiparada a Investigadora Principal do Departamento de Engenharia Mecânica da Universidade de Aveiro.

o júri / the jury

presidente / president

Prof. Doutor António Manuel de Bastos Pereira

Professor Auxiliar da Universidade de Aveiro

Doutor Ricardo João Borges Pinto

Investigador Doutorado (nível 1) da Universidade de Aveiro

Prof. Doutor António Manuel Godinho Completo

Professor Associado com Agregação da Universidade de Aveiro (orientador)

agradecimentos / acknowledgements

Ao Professor Doutor António Completo que foi o principal mentor deste projeto e cuja orientação e disponibilidade consistente ao longo do semestre foram essenciais à realização da dissertação. À Professora Doutora Paula Marques pela disponibilidade sempre que necessário ao longo do semestre. Aos investigadores do TEMA (Centre for Mechanical Technology and Automation) pela disponibilidade em ajudar sempre que necessário durante o tempo passado nos laboratórios.

A todos os meus amigos que, da melhor forma, influenciaram o meu percurso académico. Sem eles a conclusão desta etapa não teria sido preenchida de tão bons momentos.

Por último, um enorme agradecimento à minha família que sempre me apoiou a todos os níveis e sem eles seria impossível completar esta jornada.

A autora agradece o apoio financeiro através do projeto POCI-01-0145-FEDER-028424 - PTDC/EME-SIS/28424/2017, financiado pelo Programa Operacional para a Competitividade e Internacionalização (COMPETE 2020) nas suas componentes FEDER e Fundação para Ciência e Tecnologia (FCT) através do orçamento de estado (OE). A autora agradece o apoio financeiro através da bolsa FCT UID/SEM/0048/2019-FCT e a Infraestrutura de suporte CENTRO-01-0145-FEDER-022083 - Centro Programa Regional (Centro2020).

keywords

Electrospinning equipment, Tissue Engineering, Nanofibre Alignment, Cartilage, Biofabrication, Design of Experiments, Scaffolds, Biomechanics

abstract

This dissertation had as main objective the implementation of an experiment plan for an automated electrospinning system in the field of Tissue Engineering, with main focus on cartilage tissue, as well as the development of a tool capable of predicting the dimensional characteristics of the tissue mesh, depending on the controllable input parameters of the system. In an initial stage, the main structural features of the cartilage tissue, as well as its components and biomechanics. In a second stage, information about the various biofabrication technologies applied to tissue engineering was compiled, focusing primarily on the electrospinning process and the referent techniques used to control the orientation of the fibres. Further ahead, having as base the functioning of the automated electrospinning system, the design of experiments (DoE) was created. For the DoE, three input factors were considered, them being the flow rate, the velocity of the collector bands and the linear velocity of the deposition table. The output variables of the resulting electrospun fibres were the fibre diameter, the space between the fibres and the size of the pores. For each input factor, two levels were considered (low and high), which originated a 2-level factorial design with a total of 2^3 experiments to be conducted. It was used replication in the DoE in order to achieve better results, so the total number of trials realised was sixteen, and the polymer used was PCL/Gelatin.The fibre meshes generated for each experiment were then submitted to a scanning electron microscope (SEM), and the output variables were quantified. The dimensional results of the meshes were statistically analysed (ANOVA), the effects of each parameter, and the interaction between them was determined, as well as its statistical significance. Complementary to this, an equation was developed in order to predict the output variables' dimensions with respect to the input variables. This equation was then compared with both the experimental results and the theoretical model previously defined. In conclusion, the three input factors showed significant influence on the space between the fibres and the pore size. However, it is possible to verify that the velocity of the deposition table has a much higher effect on the space between the fibres than the velocity of the collector bands and the flow rate. It is also verified that there's a significance interaction between most of the input factors in both the space between the fibres and the pore size.

palavras-chave

Equipamento de eletrofiação, Engenharia de tecidos, Alinhamento de nanofibras, Cartilagem, Biofabricação, Plano experimental, *Scaffolds*, Biomecânica

resumo

Esta dissertação teve como objetivo a implementação de um plano de experiências com recurso a um sistema automatizado de eletrofiação para a engenharia de tecidos de cartilagem, assim como o desenvolvimento de uma ferramenta de previsão das características dimensionais da malha eletrofiada em função de diferentes parâmetros controláveis do sistema automatizado. Numa primeira etapa deste trabalho clarificaram-se as principais características estruturais do tecido de cartilagem, assim como a sua organização e biomecânica. Numa segunda etapa compilou-se informação relativa às tecnologias de biofabricação aplicadas à engenharia de tecidos de cartilagem com particular enfâse no processo de eletrofiação e respetivas técnicas para orientação de fibras. De seguida, e com base no princípio de funcionamento do sistema automatizado de eletrofiação, desenvolveu-se um plano de experiências (DoE). Para este plano foram definidos os três fatores de entrada (controláveis), sendo estes o fluxo de eletrofiação, a velocidade dos tapetes coletores, e a velocidade linear da mesa de deposição. As variáveis de resposta da malha eletrofiada foram o diâmetro da fibra, a distância entre fibras e o tamanho de poro da malha. Para cada fator de entrada foram estabelecidos dois níveis, dando origem a uma plano de experiencia de fatorial de 2^3. Nesta fase foram definidas as combinações de valores para os 3 fatores de entrada a utilizar na eletrofiação das malhas de fibras de orientação controlada. Procedeu-se de seguida à implementação do plano de experiência no sistema de eletrofiação, foi utilizado o polímero PCL/gelatina, tendo sido realizados um total de 16 combinações dos três fatores de entrada. As malhas de fibras geradas foram analisadas com recurso a um microscópio eletrónico de varrimento (SEM) e quantificadas as três variáveis de resposta. Os resultados dimensionais das malhas produzidas foram tratados estatisticamente (ANOVA), os efeitos das variáveis de entrada e sua interação nas variáveis de resposta foram determinados, bem como a sua significância estatística. Complementarmente foi deduzida a equação de previsão das variáveis de resposta em função das variáveis de entrada. Esta equação foi ainda comparada com a equação desenvolvida tendo como base os aspetos teóricos do processo de eletrofiação e deposição do sistema automatizado. Conclui-se que os três fatores de entrada possuem influência significativa para o espaçamento entre as fibras e, consequentemente, o tamanho dos poros. No entanto, é possível verificar que o parâmetro com maior efeito na distância entre fibras é a velocidade da mesa. Verifica-se também uma forte interação entres os diferentes fatores de entrada para o espaçamento entre as fibras e para o tamanho dos poros.

Contents

List of Tables

Intentionally blank page.

List of Figures

Lista de Abreviaturas

AC Articular cartilage

ECM Extracellular matrix

DoE Design of Experiments

CNC Computer Numeric Control

PCL Polycaprolactone

TFE Trifluoroethanol

SEM Scanning electron microscope

SLS Selective Laser Sintering

SLA Stereolithography

FDM Fused Deposition Modelling

Intentionally blank page.

Chapter 1

Introduction

1.1 Objectives

The main objective of this dissertation was the implementation of an experiment plan for a fully automated electrospinning system in the field of Tissue Engineering, with main focus on cartilage tissue. Moreover, an analytical tool was to be developed with the ability to predict the dimensional characteristics of the resulting tissue mesh, dependent on the controllable input parameters. The need to identify which parameters affect the most the electrospinning results has been growing with the decades. If the results can be accurately predicted a lot of time can be saved and the goals can be achieved easily. The electrospinning equipment in use has both moving collecting and deposition modules in order to better control the fibre alignment. This equipment was designed by Prof. António Manuel Godinho Completo and was installed at the Centre for Mechanical Technology and Automation.

1.2 Motivation

In the current days, cartilage is one of the essential biomarkers in degenerative and traumatic joint diseases. The idea of creating a synthetic form of cartilage in order to treat joint diseases has always been very appealing since it would be a turning point for the scientific and medical community. When the opportunity of being involved in such a project arose, allowing me to give some contribution to the investigation in the field,

the answer could only be yes.

1.3 Dissertation Structure

This dissertation is organized into five chapters; this small introduction included. The first chapter is dedicated to a presentation of the scenario in which this dissertation is based, and its structure. In the second chapter, there is a small introduction to cartilage tissue, mainly regarding its structural features, as well as its components and biomechanics.

In the third chapter information about the various biofabrication technologies applied to tissue engineering was compiled, focusing primarily on the electrospinning process and the referent techniques used to control the orientation of the fibres. A patent database of electrospinning techniques to control the fibre orientation is presented.

Chapter four contains a detailed description of the experimental part, as well as the results and their posterior analysis. The Design of Experiments is introduced, as well as the input and output parameters. A section with images of the experimental results is also presented for a better conceptualization of the work made. The effect of each parameter is calculated as well as its interactions with each other. A theoretical model is deduced and explained to simulate the space between the fibres. Moreover, an experimental model based on a linear regression calculated with ANOVA statistical analysis is introduced, which is then compared with both the theoretical model and the actual experimental results.

Finally, in chapter five, some conclusions regarding the dissertation are mentioned and a small discussion on possible future work, and how to improve or continue this study, is made. Two appendixes also make part of the digital version of this dissertation.

Chapter 2

Cartilage

2.1 Introduction

Cartilage is a tissue that, along with the bone, forms the framework that supports the body as a whole. This tissue has an enormous biological significance since vertebrate life as it is known, would be impossible without it [1].

This chapter provides an insight to cartilage, focusing on its structure, its function and its biomechanics. Initially there's an introductory reference to the components that constitute the cartilage, followed by a description of how these components influence the properties of the different zones that form the structure of the tissue. Posterior to this, there's a reference to the different types of cartilage in the human body and the functions of each type.

Finally, the biomechanics of cartilage is analysed. Moreover, the relation between the different components of the tissue and its behaviour to specific tests is explained. This analysis is essential because it shows how the cartilage tissue behaves when submitted to various stress tests and how the collagen fibres are aligned during that response. In order to successfully recreate a structure that "simulates" cartilage, a previous insight on this behaviour is needed.

2.2 Structure, Function and Biomechanics

2.2.1 Structure

Articular cartilage is a living structure composed of a small number of cells surrounded by a dense extracellular matrix (ECM). Unlike most tissues, articular cartilage does not have blood vessels, nerves, or lymphatics [2]. The ECM is mainly constituted of water, collagen, and proteoglycans, and it represents $\sim$ 65 to 80% of the total weight of the tissue. Inside the ECM, water represents $\sim$ 80% of the total weight, collagen is $\sim$ 60% of the total dry weight and the proteoglycans are $\sim$ 10 to 15% of the total wet weight. Moreover, the chondrocytes represent only $\sim$ 2% of the total volume of the cartilage. A representation of the constituents of this tissue is depicted in Figure 2.1.

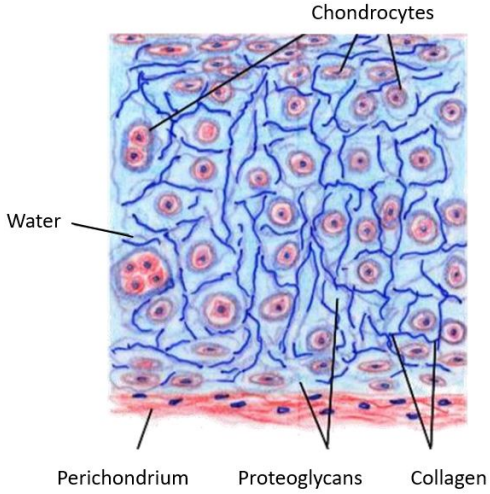

Figure 2.1: Different constituents of cartilage [3].

Chondrocytes are highly specialized, metabolically active cells that play a unique part in the growth, preservation, and repair of the ECM [2]. They are responsible for the production of the proteins that make up the ECM, as well as the metalloproteinases, which are capable of destructing the matrix. The production, organization, and maintenance of the extracellular matrix are ensured and controlled by the activity of the chondrocytes. Consequently, both the mechanical and structural properties of the cartilage are dependent on the interaction between the chondrocytes and the ECM [4].

The proteoglycans are responsible for "calling" the water molecules to the interior

of the ECM. As a person ages, the concentration of these proteins decreases and, consequently, the volume of cartilage tissue shrinks due to the significant drop in the capability to attract water. Besides this, proteoglycans also provide rigidity to the ECM, resisting compression and filling its gaps [3].

There are several types of collagen present in cartilage tissue. Type II collagen represents $\sim$ 90 to 95% of the collagen in the ECM and forms fibrils and fibres intertwined with proteoglycan aggregates [2]. Collagen fibres contain a region that consists of 3 polypeptide chains curled into a triple helix. This helix's structure provides articular cartilage with important shear and tensile properties, which also help to stabilize the matrix [3] [2].

The structure of articular cartilage is often described in terms of four zones, as it's represented in Figure 2.2. They are located between the articular surface and the subchondral bone and are the following: the tangential zone, the intermediate zone, the deep zone, and the calcified zone. The differences between them rely simply on the different orientation of both the chondrocytes and the type II collagen fibres. Furthermore, each region also has a unique extracellular matrix composition and chondrocytes with different metabolic properties [4].

The tangential zone protects the deeper layers from shear stresses, and it makes up approximately 10 to 20% of the articular cartilage thickness. This layer has a relatively high number of flattened chondrocytes, a high percentage of collagen fibres – mostly type II and IX – and a small number of proteoglycans. The collagen fibres are packed tightly and are parallelly aligned to the articular surface [2]. This disposition of the elements, along with their activity, allows this surface to act as a permeable membrane to bigger molecules, as an antibody of the synovial fluid to the cartilage, and also as a barrier to the tensions executed on the structure. This zone is the richest of all in collagen fibres and cells; however, the reduced metabolic activity of the chondrocytes makes it harder to occur regeneration. Thus, any injury or degenerative process that occurs in this zone will affect the adjacent layers. [4].

The intermediate zone provides an anatomic and functional bridge between the superficial and deep zones, and it represents about 40 to 60% of the total cartilage volume [2]. In this layer, the collagen fibres and the chondrocytes are randomly disposed

of in the matrix. The chondrocytes are spherical and appear in a lower density than in the tangential zone; however, its metabolic activity suggests a higher ability to regenerate. Functionally speaking, the intermediate region is the first line of resistance to compressive forces [2].

The deep zone provides the most significant resistance to compressive forces because the collagen fibres are arranged perpendicularly to the articular surface, and it represents about 30 to 40% of the articular cartilage volume [5]. This layer contains the highest diameter collagen fibrils radially disposed of, the highest proteoglycan content and the lowest water concentration. It plays an important role when it comes to weight support and shock absorption by the cartilage. Unlike the tangential zone, which is designed to resist shear stresses, the deeper layers are more fit to resist traction and compression forces, due to the orientation of the collagen fibres and the high concentration of proteoglycans [4] [5].

There's a spline line that separates the deep and the calcified zone, commonly known as "*Tidemark*". It consists of a strip of powerful collagen I fibrils that allow the fixation of the collagen II fibrils which, then, extend to the deep zone [4]. The calcified zone plays an integral role in securing the cartilage to the bone, by anchoring the collagen fibrils of the deep zone to the subchondral bone. In this area, the population of cells is scarce, and chondrocytes are hypertrophic, however, despite their low concentration, they're responsible for the mineralization of the matrix, providing an excellent interface for the incorporation of the bone tissue [2] [5].

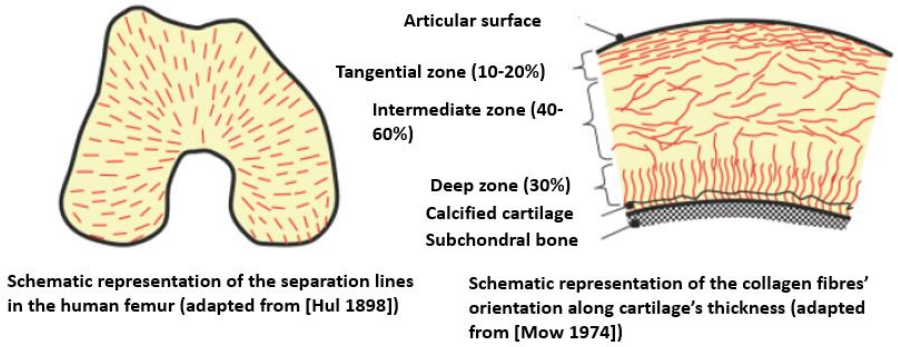

Figure 2.2: Scheme of the different zones of cartilage [3].

2.2.2 Function

Cartilage function can vary during the life cycle. In the embryo, it provides support and is a foundation to the bone. Embryonic cartilage either remains as cartilage or provides a substructure for endochondral ossification; this last part means that it also functions as a guide for the rapid growth and development of the musculoskeletal system [6]. Articular cartilage's primary function is to provide a smooth and lubricated surface for low friction articulation and to facilitate the transmission of loads to the underlying bone [2].

There are different types of cartilage in the human body and, even though their components are very similar, their quantities differ, which causes the cartilage to have distinct qualities, and consequently, different functions. The most common form of cartilage is called hyaline, which is the embryonic form of cartilage, also found in the ribs, joints, nose, larynx, and trachea [6]. It consists of fine collagenous fibres embedded in a solid gel substance and, it's this structure that gives hyaline cartilage good strength and flexibility. It's the primary structural cartilage of the human body and is used to replace bone wherever greater flexibility is needed [7] [8].

Fibrocartilage is another type, and it is found where the tendons and ligaments meet the bone – at the pubic symphysis, in the menisci and the centre of the intervertebral disc [6]. Besides being a highly flexible tissue, a quality that is reinforced by the parallel alignment of the collagen fibres [6], it is also sturdy and has a significant tensile strength.

Elastic cartilage is the least common type of cartilage found in the human body. This type of cartilage is not very strong when compared to the hyaline cartilage; however, it is much more flexible and has some elasticity [9]. Elasticity is the ability a substance has of returning to an initial form after suffering deformation, and because of this, elastic cartilage is mainly found in areas where this property has the most importance. The anatomic parts that are always required to spring back into their original shape are, for example, the outer part of the ear and the epiglottis [6].

2.2.3 Biomechanics

Articular cartilage is subjected to repeated cycles of compressive and shear loads during daily activities. Normally, an individual will take around 1 to 4 million steps

in a year in which their joints are subjected to periods of both, rest and motion [10]. In the specific case of the knee, for example, the distal femur contacts, rolls, and slides across the tibial plateau during around 60% of the walking cycle, with a contact area of $\sim$ 3-4 cm^2 during knee flexion. Joint surfaces also slide across each other in the relative velocity of $\sim$ 0.2 m/s [11]. Taking this into consideration, it's easy to conclude that, throughout a person's lifetime, articular cartilage endures a high biomechanical demand, in both compression and shear [12]. This tissue provides bearing support with low friction and wear. Because of its compliance, it helps to distribute the loads between opposing bones in, for example, a synovial joint, represented in Figure 2.3. If cartilage were a rigid material like bone, the contact stresses at a joint would be much higher, as the contact area would be much smaller [12].

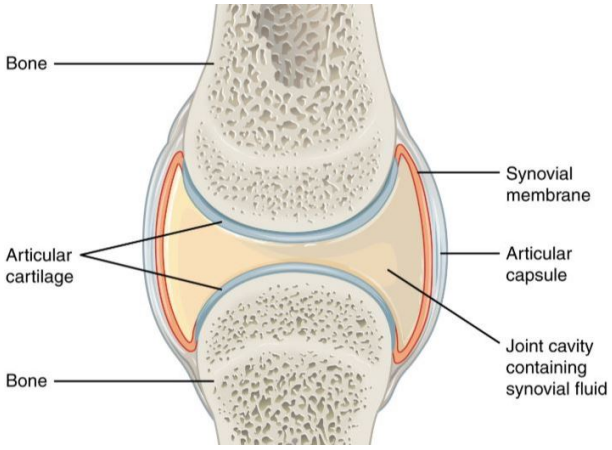

Figure 2.3: Constitution of Synovial joint [13].

Cartilage in compression

When submitted to compression loads, cartilage suffers a decrease in its thickness - deformation. Currently, there are several tests to determine the properties of cartilage when subjected to compression, but, the most frequent ones are the confined compression, unconfined compression, and the indentation test, as represented in Figure 2.4.

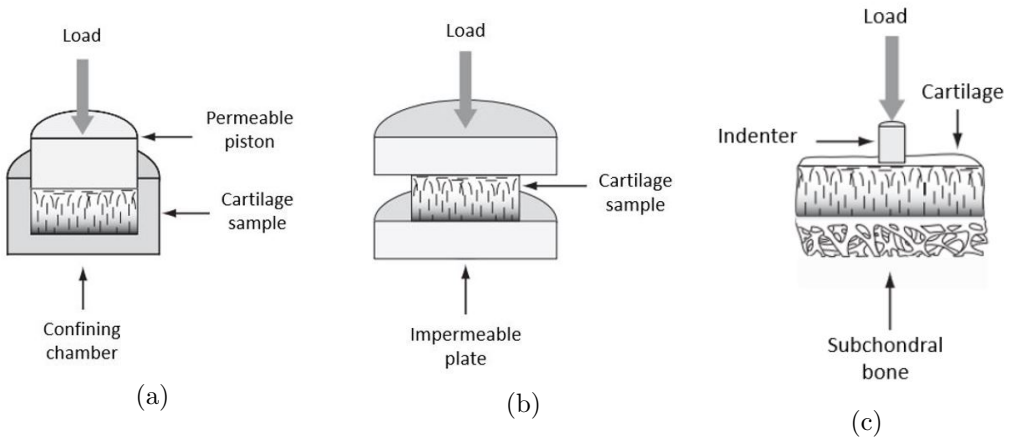

Figure 2.4: Schematic representation of common experiments applied to articular cartilage: (a) Unconfined compression, (b) Confined compression, (c) Indentation. Adapted from [14].

The material properties of cartilage are usually determined with a confined or unconfined compression test. Confined compression is used either in a "creep" mode or in a "relaxation" mode. In the first one, a constant load is applied to the cartilage through a porous plate, and the displacement of the tissue is measured as a function of time [12]. In the second method, a constant movement is applied to the tissue, and the force needed to maintain the same displacement is measured [3].

In creep mode, the cartilage deforms under a constant load; however, the deformation is not immediate, as it would be in an elastic material. The displacement is a function of time, as the fluid cannot escape from the matrix instantaneously [12]. At first, the displacement is fast, which corresponds to a comparatively large flow of fluid out of the cartilage. As the rate of movement slows down, and the displacement approaches a constant value, the fluid flow also reduces. Finally, in an equilibrium state, the displacement is constant, and the fluid flow stops. When the state of equilibrium is achieved, two properties of the cartilage can be determined – the aggregate modulus and the permeability [15]. The aggregated modulus evaluates the stiffness of the cartilage when the flow of fluid ceases. Thus, it can be concluded that the higher the aggregate modulus, the less the cartilage deforms under a given load [12]. The standard value of this modulus, for cartilage, varies between 0.1 and 2 MPa [16].

The permeability of cartilage can also be determined using a confined compression test but in the relaxation mode. In the relaxation mode, the load applied to the articular

surface is balanced by the compression load, generated inside the solid matrix, and the resistance to the fluid flow through the matrix [3]. The relaxation of the tissue ends when the applied load is balanced only by the created compression loads in the solid matrix. Permeability indicates the resistance to fluid flow through the cartilage matrix [12]. The fluid's velocity can be described according to Darcy's Law, represented in Equation 2.1, where k represents the permeability, and the pressure gradient is approximated by Equation 2.2.

$$v_{ave} = k \cdot \nabla p \tag{2.1}$$

$$\nabla p \simeq \frac{P_2 - P_1}{h} \tag{2.2}$$

Permeability is not constant through the entire cartilage tissue and its value, for this tissue, usually varies between 10^{-15} to $10^{-16} m^4/N \cdot s$ [12]. In articular cartilage, the permeability is higher near the joint surface – fluid flow is relatively easy – and lower in the deep zone – fluid flow is more difficult [12]. Hence, as a joint is loaded, most of the fluid that crosses the articular surface comes from the cartilage closest to the joint surface [3]. Permeability also varies with the tissue deformation and with the pressure of the interstitial fluid; thus, when the cartilage is compressed, the deformation rate increases and the permeability drops exponentially [12]. The same behaviour can be observed if the pressure of the interstitial fluid is increased, as demonstrated in Figure 2.5. This reduction of permeability is a result of the compaction of the solid matrix, which decreases the porosity and originates a higher frictional drag force on the fluid inside the matrix [3].

Permeability's non-linearity, represented in Figure 2.5, suggests that articular cartilage holds a feedback system, which is extremely important in severe physiological conditions. Its dependence on the degree of deformation in the tissue constitutes a valuable mechanism to maintain the distribution of load between the liquid and the solid phase of the cartilage. If the fluid flows smoothly through the membrane, the solid matrix will endure, entirely, the contact loads, which makes it more prone to damage.

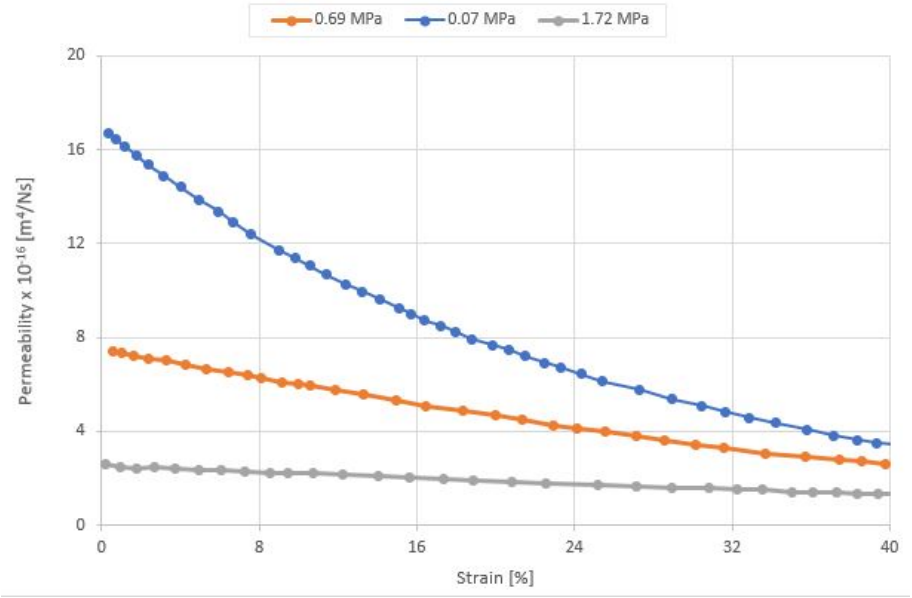

Figure 2.5: Representation of the usual behaviour curves of permeability when subjected to different levels of deformation at different pressures in articular cartilage. Adapted from [17].

An excellent alternative to the confined compression test, used to evaluate the permeability of cartilage, is the indentation test (Figure 2.4c). Using an indentation test cartilage can be tested *in situ*, which is the closest condition to the physiological state. Unlike the confined compression, the cartilage remains attached to its underlying bone, which provides a more natural environment for testing [12]. Typically, an indentation test is performed under a constant load, and the diameter of the indenter varies according to the curvature of the joint surface, but, usually, it's around 0.8 mm. Besides permeability, this test also allows the determination of Young's modulus (E) and the Poisson's ratio (ν). In equilibrium, the typical values for Young's modulus vary between 0.41 and 0.85 MPa [3], while the Poisson's ratio varies between 0.06 and 0.18 [18]. Previous studies assumed cartilage as an incompressible material, and, as such, a Poisson's ratio of 0.5. This assumption was based on the fact that cartilage is mainly composed of water, which is, normally, modelled as an incompressible fluid. However, this hypothesis is not the most accurate, since when a load is applied to the tissue, there's a flow of fluid leaving the solid matrix, reducing the volume of cartilage.

Cartilage responds as a uniformly linear-elastic solid to rapid load changes, with Young's modulus of $\sim$ 6MPa [18]. For slower load changes, such as in the march cycle,

cartilage shows non-linear compression properties [19].

Cartilage in tension

Cartilage is a complex material with anisotropic properties that are determined by the zonal differences in the content and orientation of collagen, its main structural constituent [20]. A study on glenohumeral cartilage, made by Huang *et al.* [21], determined Young's modulus under tensile strength of 3.5 MPa in the direction of the split-lines, while the value obtained in the perpendicular direction to the split-lines was 4.5 MPa. Under elevated values of deformation, this modulus can go up to 45 MPa and 25 MPa in the parallel and perpendicular directions to the split-lines, respectively. The stiffness of cartilage also varies along with its thickness, and for mature animals, it is more rigid near the articular surface [22]. In contrast, in the case of an immature skeleton, the cartilage becomes more rigorous in its deep zone. The anisotropy of cartilage is related to the organization of the collagen fibres and proteoglycans in the tissue [23]. The existence of an abundant quantity of collagen in the cartilage's surface, and its parallel orientation to the articular surface, gave cartilage a thin layer that is very resistant to wear [3].

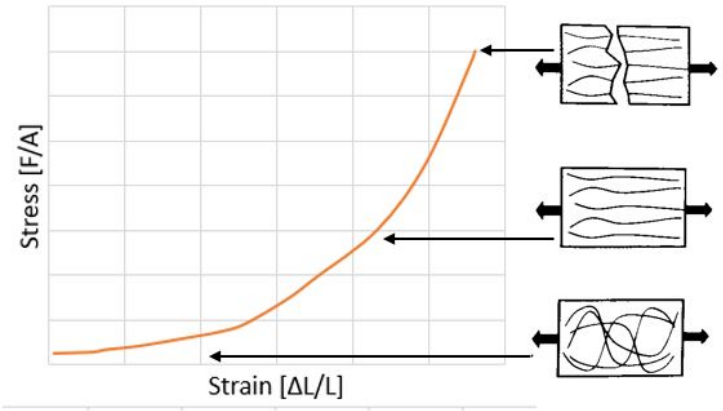

Figure 2.6: Typical stress-strain curve of cartilage submitted to an uniaxial tensile load and the respective orientation of the collagen fibres. Adapted from [14].

Cartilage shows a viscoelastic behaviour, which is due to the movement of the interstitial fluid in the porous structure of the solid matrix, as well as the interaction with friction between the collagen fibres and the network of aggregated proteoglycans. Thus,

when the cartilage is submitted to a tension test at low velocities, the stiffness and resistance to traction properties depend only on the collagen network. Figure 2.6 shows the stress-strain characteristic curve in a uniaxial tension test, at low velocities. It is perceptible that cartilage tends to become more rigid as the deformation increases [3]. The tangential line to the stress-strain curve represents the stiffness of the tissue, and it can vary between 3 to 100 MPa [22] [3].

The way the stress-strain curve is shaped is related to the organization of the collagen fibres in the solid matrix. The first zone is associated with the non-alignment of the fibres with the direction of application of the force. In this first phase, the movement of alignment of the fibres occurs without opposing the deformation at all. However, both the next and the final stage, are dominated by the resistance of the collagen fibres to strain, and, since the fibres are already aligned, if the load applied is too high, it can lead to the rupture of the tissue.

Cartilage in pure shear

In compression and tension, the properties that are inherent to the solid matrix can only be determined in an equilibrium state, since the volumetric alterations that occur in the cartilage induce a viscoelastic effect in the tissue. However, if the cartilage is tested in pure shear, at low levels of strain, the pressure gradients are no longer generated in the tissue, since the flow of the interstitial fluid no longer occurs [24], as illustrated in Figure 2.7b. Besides this, the interstitial fluid is water, which has a very low coefficient of viscosity. Thus, it doesn't have a significant contribution to shear resistance [3], making the solid matrix the only one responsible for it. A steady dynamic pure shear can be used to determine the intrinsic viscoelastic properties of the collagen-proteoglycans solid matrix. Usually, thin circular wafers of tissue are subjected to a steady sinusoidal torsional shear, secured by two platens that induce a small compression load in the sample. The process is illustrated in Figure 2.7a. The lower platen allows the measuring of the torque applied, and the upper platen measures the angle used on the sample. The sinusoidal movement applied to the sample varies between 0.01 and 20 Hertz (Hz) [25].

The measure of total resistance offered by the viscoelastic material is called dynamic shear modulus. The phase shift angle is the measure of total energy dissipation within

the material.

A study made by Zhu *et al.* [24] showed that the values of the dynamic shear modulus vary between 1 and 3 MPa, in bovine cartilage, and the values of the phase shift angle between 9°and 20°. The same experiment was done with solutions containing a concentration of proteoglycans similar to the articular cartilage, and the results were 100 times inferior to the ones obtained in the first experiment. This data proved that shear stiffness in articular cartilage comes from the collagen and the interaction between the collagen and the proteoglycans, and not from the proteoglycans itself [26].

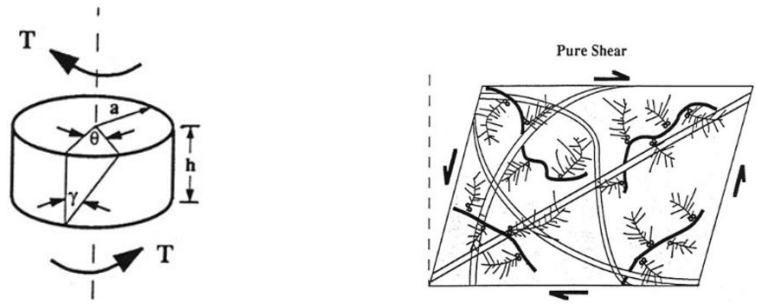

(a) (b)

Figure 2.7: (a) Schematic representation of a shear test being performed. (b) Schematic representation of cartilage subjected to a pure shear load. Adapted from [25].

Mechanical properties of cartilage and its composition

The compressive stiffness of the cartilage increases with the amount of glycosaminoglycans [27], as it can be observed in the graph in Figure 2.8. In these cases, compressive stiffness is measured in relaxation mode 2 seconds after the load is applied [3]. Both permeability and compressive stiffness, measured by the aggregate modulus, are highly correlated with the water content - as the latter increases, the cartilage becomes less rigid and more permeable, as shown in Figure 2.8. Samples gathered from the articular surface show more stiffness than samples from the deeper zones of cartilage. This can be explained by the fact that in the articular surface, there is a higher concentration of collagen parallelly aligned to the surface.

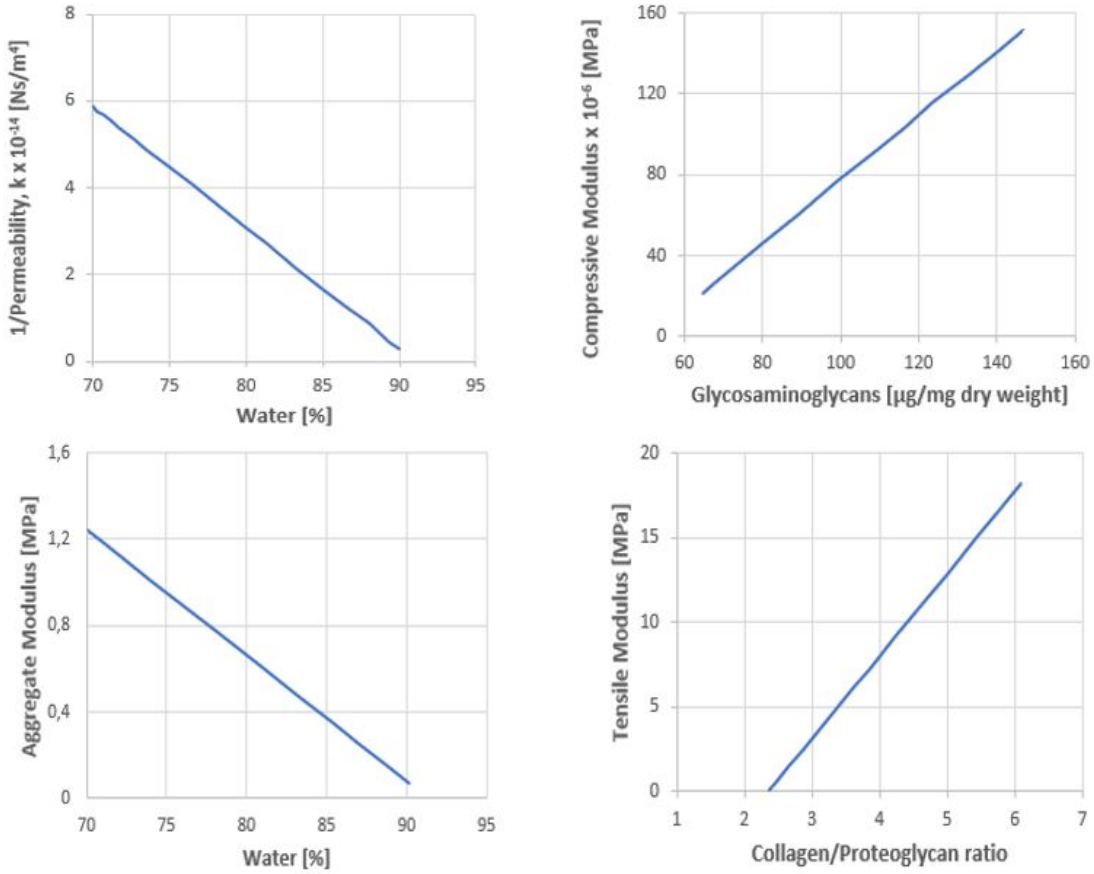

Figure 2.8: Typical correlation curves between the different properties of cartilage and its composition. Adapted from [27] [28] [29].

The decrease in the proteoglycans amount allows the creation of more space in the tissue for the fluid. Increasing the amount of water will consequently increase the permeability of the membrane, and the rise of the latter allows the fluid to flow through the tissue more efficiently, which results in a higher rate of deformation [3].

In summary, as it can be evidenced by the previous explanation, cartilage's fibrillar organization is of great importance since it is responsible for its unique mechanical properties. Thus, in order to successfully create a synthetic tissue that achieves an excellent level of similarity with the biological tissue, it is essential to replicate the fibrillar organization of the native tissue in question. This has proven to be effectively achieved with the electrospinning technology, by developing fibrous scaffolds for tissue engineering in cartilage, since aligned polymeric nanofibres matrices mimic the topography of the native tissue's ECM [30].

Intentionally blank page.

Chapter 3

Biofabrication in Tissue Engineering

3.1 Introduction

This chapter focuses on the reality that is tissue engineering and biofabrication, exploring the different techniques and materials used in this field.

Tissue engineering emerged in the mid-1980s and has continued to evolve as a multidisciplinary field. Its focus is on cells, scaffolds, nutrients, and growth factors, intending to repair, or replace, the tissue in damaged organs [31].

Damaged articular cartilage has a low capacity of regeneration due to its low vascularization. It also has a limited natural tendency to spontaneous repair. Thus, even the smallest traumas can lead to cartilage deterioration as time passes by. Cartilage's low ability to self-repair made it the ideal candidate for tissue engineering and some of the strategies used involve biomaterials seed with chondrocytes or stem cells.

Biofabrication is often defined as the production of complex biologic products from raw materials such as living cells, matrices, biomaterials, and molecules [32]. This technology evolved, and is still changing, rapidly, and has been stimulated by the development of 3D fabrication technologies. Electrospinning is probably the most effective biofabrication technique to produce synthetic cartilage since it is capable of providing highly-aligned nanofibres which is essential to replicate the native tissue's mechanical properties.

3.2 Processes and materials in scaffolds fabrication for cartilage's engineering

3.2.1 Scaffolds

The definition of scaffold is categorized into two main categories – a cell delivery scaffold and a drug delivery scaffold. The first one is relative to when cells are implanted into an artificial structure capable of supporting three-dimensional tissue formation. The second is comparable to when drugs are loaded into a 3D artificial porous structure capable of high drug loading efficiency. A scaffold is typically made of polymeric biomaterials, and it provides structural support for cell attachment and, consequently, tissue development [33]. In Figure 3.1, there's a representation of different types of scaffolds designs used in tissue engineering.

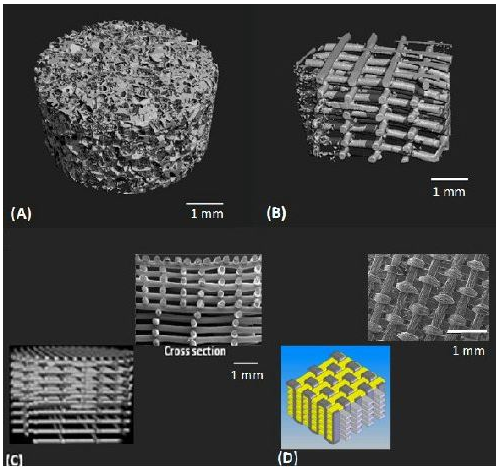

Figure 3.1: Different scaffold structural designs for cartilage tissue engineering: (A) 3D sponge; (B) fibrous; (C) gradient; and (D) woven [34].

The best scaffold for an engineered tissue should be the ECM of the targetted tissue in its native state; however, the complex composition of the matrix in native tissues makes it difficult to replicate it exactly. As a result, the crucial roles played by scaffolds in engineered tissues are similar to the ECM's function in native tissues and are related to their architectural, biological, and mechanical features [31].

Whatever the tissue type, a few key factors are essential when designing a scaffold to be used in tissue engineering, and they are listed below.

Biocompatibility

The scaffold must be biocompatible – cells must adhere, function normally. After implantation, the structure, or tissue-engineered construct, must produce a small immune reaction to prevent it, causing a severe inflammatory response that could cause rejection by the body, or reduce healing.

Biodegradability

The main objective of tissue engineering is to allow the body's cells, over time, to replace the implanted scaffold. Thus, it's essential that scaffolds are biodegradable so that cells can produce their own extracellular matrix. The by-products of this degradation must be non-toxic and able to exit the body without interfering with other organs [33].

Mechanical and Physical Properties

Ideally, the scaffold should have mechanical properties that are consistent with the anatomical location into which it's implanted [33]. Producing scaffolds with adequate mechanical properties is still one of the significant challenges in attempting to engineer bone or cartilage tissue. For these tissues, in specific, the implanted scaffolds must have enough mechanical integrity to function from the time of implantation to the conclusion of the remodelling process.

Architecture

In cartilage tissue engineering, scaffolds are expected to imitate the functions of damaged cartilage and provide a 3-dimensional (3D) environment for cell growth and ECM production. Thus, the architecture of scaffolds has critical importance in tissue engineering. Scaffolds must provide an empty volume for vascularization, new tissue creation, and remodelling [35]. Hence, these structures must have highly interconnected pores, and the size of these pores must be, at least, a bit larger than the cells that will be seeded on them. This will guarantee there's enough space for the entry and exit of nutrients and residues, respectively. Usually, the values of desirable porosity are 90% with sizes varying between 20 and 220 µm [35]. The achievement of this kind of porosity is highly connected with the space between the fibres since the size of the pores totally

depends on the latter. This is the most important characteristic of a 3D structure since, the ability to control the organisation of the fibres is what makes it possible to recreate fibrillar organisation of cartilage.

3.2.2 Biofabrication Processes

There are numerous techniques for scaffold fabrication. The conventional ones – solvent casting, phase separation, gas foaming – involve different processes to obtain high porosity structures and were the first to be used in tissue engineering. These are straightforward techniques; however, they don't allow precise control over the dimensions, geometry, pore distribution and interconnectivity, which makes them not the most suitable for the 3D fabrication of scaffolds [36]. Moreover, they are arduous techniques that involve solvents, mostly organic, which sometimes are toxic to the cells. Thus, these techniques are preferentially used for scaffold production using polymeric materials [37]. Nowadays, the most common techniques for 3D Biofabrication are ink-jet printing, fused deposition modelling, stereolithography (SLA) and selective laser sintering (SLS). Each of these techniques has advantages and disadvantages that should be considered, however, they allow the production of scaffolds with controlled geometry, guarantee uniformity in the pores distribution and their interconnectivity, while not requiring a lot of human intervention nor the use of organic solvents.

Conventional Techniques

Solvent Casting/Salt Leaching

This technique involves using a polymer solution uniformly mixed with salt particles of a specific diameter [38]. The solvent evaporates, leaving behind a polymer matrix with salt particles incorporated in it. The composite is then immersed in water, and the salt dissolves, producing a porous structure, as it can be seen in Figure 3.2. This technique allows the production of highly porous scaffolds with porosity values up to 93% [38]. Its primary disadvantage is the fact that it can only be used to produce thin membranes, no thicker than 3 mm, which makes it harder to fabricate 3D structures.

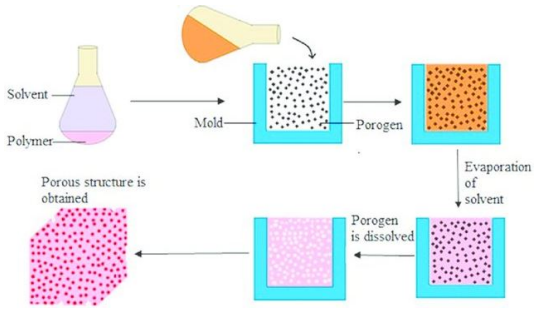

Figure 3.2: Schematic representation of the Solvent Casting/ Salt Lecahing technique. Adapted from [39].

Gas Foaming

In this process, moulded biodegradable polymers are pressurized at high pressures with gas foaming agents - like CO2 and nitrogen (N), water, or fluoroform [38]-, until the polymers are saturated, as shown in Figure 3.3. The result of this technique is the growth of gas bubbles, with sizes between 100 and 500 µm [33], in the polymer. The main advantage of this process is the fact that it is an organic solvent-free process [38]. In opposition, its main disadvantage is that this process can produce a structure with unconnected pores and a non-porous external surface [33].

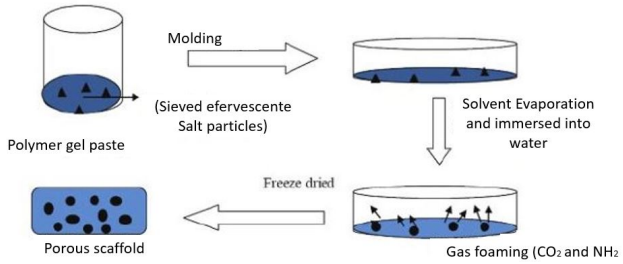

Figure 3.3: Fabrication of scaffold using the gas foaming method. Adapted from [33].

Phase Separation

Phase separation, represented in Figure 3.4, is a solution-based technique that allows the creation of highly porous scaffolds [40]. The solution is prepared in a container and subsequently placed in a freezer. The temperature drops radically, and this causes the solvent to crystallise and freeze, inducing a solid-liquid phase separation. The solidified mixture is then transferred to a freeze dryer, where the solvent is removed from the

mix by applied vacuum. The fact that the process is conducted at low temperatures is beneficial for the incorporation of bioactive molecules in the structure being formed [38]. Its drawbacks include the use of potentially toxic solvents, lack of control over internal architecture, and limited range of pore sizes [33].

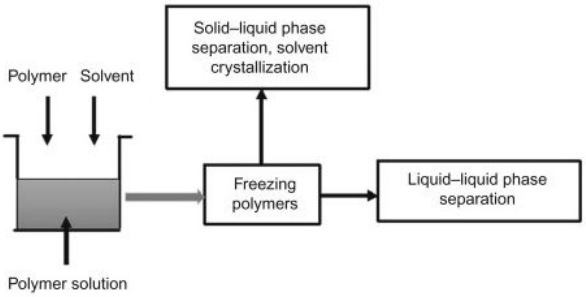

Figure 3.4: Schematic of the Phase Separation technique. Adapted from [40].

Advanced Biofabrication Techniques

Inkjet Bioprinting

Inkjet printing is a non-contact technique that refers to the spatially controlled dispensing of a jet of small beads of liquid material through a small orifice onto a substrate [41]. The liquid material is known as bio-ink, and it's made of cell culture medium or hydrogel. The volume of the bead varies between 1 and 100 pl, which is equal to 1-30 µm [42]. Currently, there are two types of inkjet bioprinting: thermal inkjet bioprinting and piezoelectric inkjet bioprinting. Both types offer an inexpensive, high-throughput capability, with the benefits of high resolution, reproducibility, and ease of use [41].

In thermal inkjet printing, represented in Figure 3.5 (A), small volumes of the printing fluid are vaporized by a micro-heater to create the pulse that expels beads from the print head [41]. The generated heat can go up to 300°C, and the resultant evaporation can result in stress for the deposited cells. Because the temperature is only applied in the bead formation stage, which lasts less than 3 µs, the extreme heat does not have a considerable impact on the viability of the cells, nor the stability of biological molecules [41].

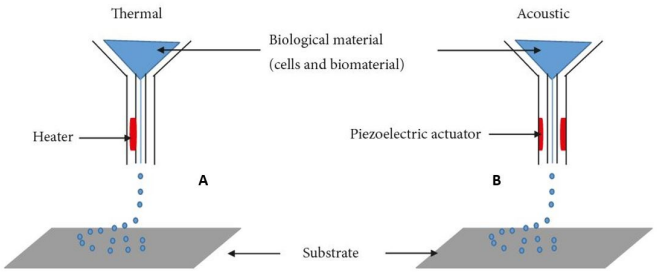

Figure 3.5: (A) Thermal inkjet bioprinting; (B) Piezoelectric-actuated inkjet bioprinting. Adapted from [43].

In the piezoelectric inkjet bioprinting, represented in Figure 3.5 (B), no heating is used for the creation of the pulse. Thus, no damage is done to any biological compound obtained within the inks [41]. Mechanical vibration is applied to the fluid in the nozzle using a piezoelectric actuator, which causes a shock wave that forces the bio-ink to go through the nozzle [41]. This allows some control of the mechanical stress experienced by the cells during the printing process.

Inkjet printing was the first technique associated with organ printing. However, although adaptable and easy-to-use, inkjet cell printing technology is still, to date, not appropriate to the development of human-size bio constructs given issues with non-uniform beads, sparse cell density, frequent nozzle blockage and physical stresses on cells [42].

Selective Laser Sintering

Selective Laser Sintering (SLS) technique employs a carbon dioxide laser beam to thin sinter layers of powdered polymeric materials to form solid 3D objects [44]. The object is built layer-by-layer from CAD data files in the STL file format. During SLS fabrication, the laser beam is selectively scanned over the powder surface following the cross-sectional profiles carried by the slice data [44]. The interaction of the laser beam with the powder raises its temperature to the point of melting and causes the particles to be fused to form a solid mass, as shown in Figure 3.6. The next layers are built directly on top of the previous layer. The materials most used in this technique are metals, ceramics, and bulk polymers, and it is used in tissue engineering to produce bone and cartilage [44].

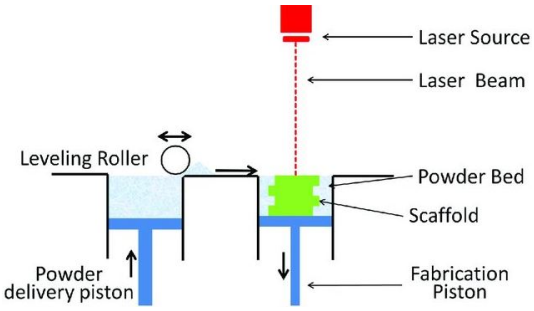

Figure 3.6: Schematic of selective laser sintering (SLS) process. Adapted from [44].

Different studies have been made over the years on how to produce scaffolds using SLS. Lee and Barlow [45] used calcium phosphate particles, coated with a polymeric material to produce scaffolds. Hao *et al.* [46] investigated the use of SLS to fabricate structures composed of hydroxyapatite and polyethylene of high density.

Its main advantages are the high accuracy it provides and the broad range of materials. The drawbacks are the elevated temperatures, the local high energy input, and the fact it does not allow the control of the porosity [44].

Stereolithography

Stereolithography (SLA) is based on the use of an ultraviolet (UV) laser that strikes a liquid medium composed of photopolymerizable material. It is a layer-by-layer form of photolithography, where the pattern is created using either a computer-controlled laser beam or a digital light projector. The photopolymerizable material is placed in a container, under a moving platform, to define each layer, as it's shown in Figure 3.7. Once the model is obtained, it must be subjected to a post-treating operation to complete the solidification process of the models, giving them maximum resistance through their exposure to intense UV radiation. After this, the model can be subjected to post-processing operations, improving its final appearance and functionality. SLA has one of the highest resolutions (5–300 µm [47]), precisions, and the softest surface finish of all plastic 3D printing technologies, but the main benefit of this technique lies in its adaptability. SLA is an excellent option for highly detailed scaffolds, requiring tight tolerances and smooth surfaces, such as moulds, patterns, and functional parts because it can achieve a spatial resolution of $\sim$ 50 µm [48].

Marketing materials used in SLA are typically epoxy-based resins that offer the ability to fabricate reliable, durable, and accurate parts with high resolution. However,

these commercial resins cannot be used as scaffold materials due to their lack of biocompatibility and biodegradability [41]. Thus, the limited selection of photopolymerizable materials has been a significant constraint for the use of SLA techniques in biofabrication for tissue engineering.

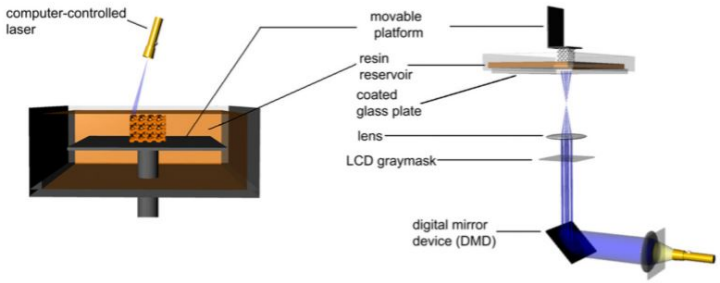

Figure 3.7: Schematic of the Stereolithography (SLA) process [41].

Fused Deposition Modelling

This technique is the second most used rapid prototyping technology, right after stereolithography. A plastic filament is disentangled from a coil and supplies material to an extrusion nozzle, as shown in Figure 3.8. The materials used in this technique are thermoplastic polymers/ceramics. The nozzle is heated to melt the plastic and has a mechanism that allows the flow of the melted plastic to be turned on and off [49]. It can be moved both in horizontal and vertical directions. As the nozzle moves over the table, it deposits a thin bead of extruded plastic to form each layer. The plastic freezes rapidly after being squeezed from the nozzle and attaches to the layer below. The entire system is enclosed in a chamber which is maintained at a temperature just below the melting point of the plastic [49].

Some of the advantages of using this technique are, for example, its low cost, its excellent mechanical strength, and the versatility in lay-down pattern design [38]. However, the extreme temperatures the process requires are view as a disadvantage, along with the small range of bulk materials [38].

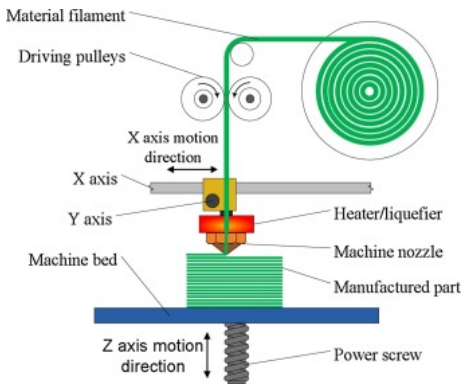

Figure 3.8: Schematic of the Fused Deposition Modelling (FDM) process [50].

Electrospinning

Electrospinning, compared with the previous techniques, is the most adequate to produce aligned fibres with the porosity needed for cartilage repair. This is a fabrication technique that uses electrical charges to draw fine fibres up to the nanometre scale [38]. It's a simple process, yet extremely useful in the production of nanofibres. In the past decades, significant developments in electrospinning have allowed for the creation of scaffolds with different materials and, thus, this technique has gained high popularity in tissue engineering research. This process can produce polymeric fibres with sizes between the order of the micrometre (10-100 µm) and the nanometre (0.01-0.1 µm) [51], which lead to the production of structures with a surface area much higher than the volume, a high porosity and a smaller size of pores. Moreover, it also has a wide range of techniques that allow the control of the fibre orientation and alignment.

The conventional electrospinning equipment consists of a high-voltage power supply, which charges the polymer solution, a syringe filled with the solution, and a grounded collector where the nanofibres are deposited. Figure 3.9 shows a scheme of the conventional vertical - 3.9 (A) and (B) - and horizontal - 3.9 (C) - electrospinning setups. Electrospinning is used to produce extra thin fibres by forcing a viscous polymer through an electric field, forming a droplet solution at the end of a metallic needle – Spinneret. The droplet at the tip of the needle suffers two opposite forces – the electrostatic repulsion and the surface tension. When the electrostatic repulsion starts to overcome the surface tension of the fluid, the pendant droplet at the tip of the needle will deform into a conical droplet, commonly known as the Taylor cone. [51] Once the Taylor cone

is formed, the charged liquid jet is ejected towards the collector. During that trajectory, the molecules of polymers are stretched, and the solvent evaporates, forming the fibres that are deposited in the collector.

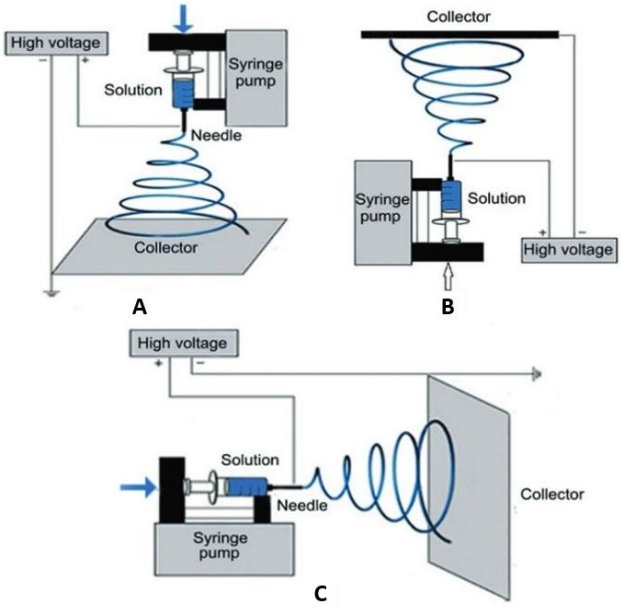

Figure 3.9: Electrospinning types and its components. Adapted from [50].

The main advantage of this technique is its versatility. There are a lot of morphologies that can be achieved just by varying the setup of the equipment and the parameters of the process [51]. Depending on the different configurations, aligned, porous, and hollow nanofibres can be created [52] [53] [54]. Besides this, several studies brought progress in the knowledge of the parameters that rule the electrospinning process. However, the optimization of the electrospinning system is still very laborious due to the high number of settings that can affect its performance and the dependence existent between them [51].

3.3 Electrospinning – Processes and techniques for fibre orientation

Fibres produced by the electrospinning technique were usually randomly aligned. However, in the past decade, various studies showed that new, innovative, configurations of the electrospinning system had been developed to keep the fibres aligned [51].

In tissue engineering, aligned nanofibres have demonstrated the ability to modulate cell behaviours such as cell shape, migration, differentiation, and extracellular matrix assembly [55]. The ability to produce aligned nanofibres is highly relevant when producing a synthetic tissue that can accurately simulate the mechanical properties of cartilage's native tissue. Electrospinning usually consists of two regimes of jet movement upon the jet emitting from the Taylor cone, this is, a segment of a stable jet in a straight line for a short distance, followed by the dominant and complex whipping motion [55]. There have been some attempts to control the spatial orientation of the fibres based on the unstable jet, mainly by altering the collector or by controlling applied forces externally. However, it would be highly advantageous to fabricate aligned fibres by making use of the segment of stable jets in electrospinning.

Electrospinning is usually conducted in the far-field mode, using a hollow needle as spinneret and a piece of metal (aluminium foil) to function as a collector [56]. This setup is generally used to produce nanofibres in a small volume. When whipping instability is involved, it is difficult to accurately control the morphology of the nanofibres [56]. Given this, modifications to the original setup have been made to enhance the capability and versatility of electrospinning. Decreasing the distance between the spinneret and the collector makes it possible for the electrospinning to be conducted in the near field, and thus, to collect the fibres from the straight segment of the jet. Using a set of needles (multiple needle electrospinning) instead of just a single needle has also been used to increase the productivity of electrospinning. Instead of using a hollow needle, a flat plate or a 2D array of solid pins with a large area surface (needleless electrospinning) has been used to raise the number of jets and, consequently, the production volume [56]. The use of a co-axial needle also allows electrospinning to produce nanofibres from unspinnable materials and to generate nanofibres with a core-sheath.

3.3.1 Methods of Electrospinning

Near Field Electrospinning

During the electrospinning process, the distance between the spinneret and the collector determines the state in which the fibres will be deposited on the collector. Near field electrospinning, illustrated in Figure 3.10, allows a better fibre deposition, combin-

ing the average velocity of the jet with the relative velocity between the spinneret and the collector; however, the diameter of the fibres is still substantial. When compared to the far-field electrospinning, near field electrospinning offers a broader range of advantages. With near field electrospinning, the applied tension can be reduced, it is possible to organize the fibres in a large area and with more precision, and there is the chance to manipulate the spatial positions of the fibres along with three directions [57] [58]. However, the liquid flow rate in a near field electrospinning process is relatively low, which causes a substantial reduction in the volume production [57] [58].

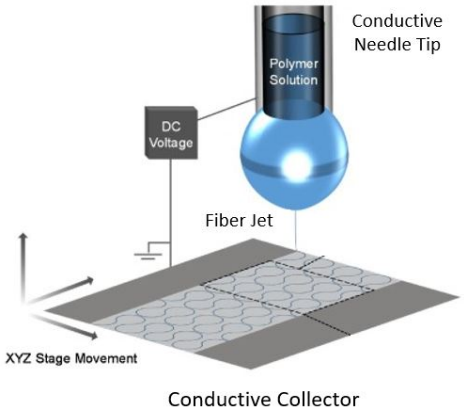

Figure 3.10: Near field electrospinning. Adapted from [59].

Multiple Needle Electrospinning

Multiple needle electrospinning offers a direct route to increasing productivity using a series of hollow needles. The needle can be disposed of in a linear matrix, organized in a straight line, or a 2D matrix, disposed of in a particular layout, [60] as illustrated in Figure 3.11. Multiple jets can be ejected simultaneously by the needles, using this setup. The trajectories of the jets are usually very irregular due to the interaction of the external electric field, the auto induced interactions and the repulsion between the jets [61]. When using the multiple needle electrospinning, it is essential to take into consideration a set of parameters, as the spacing between the needles, the number of needles and the layout of the matrix [62]. An auxiliary electrode can be placed near the needles to generate a secondary electric field between the needles and the electrode, which neutralizes the repulsion between the jets and improves the stability of the jets.

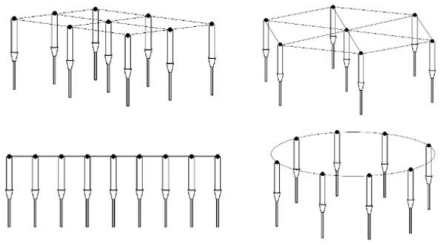

Figure 3.11: Examples of different needle dispositions [63].

Hollow and Co-axial Needle Electrospinning

Another method of electrospinning consists in the use of hollow and/or solid spinnerets. The hollow spinneret, such as a hollow needle or a tube with holes, is associated with an involucrum, from which the liquid is extruded. The solid spinneret, such as a solid pin, a 2D matrix of solid pins, and a plane substrate, allows that multiple jets can emanate at the same time from the surface for electrospinning. [56] The solid pin can be used as a spinneret to eject a jet from the liquid droplet stuck at the end of the pin [64]. A flat plate was also explored as the spinneret to increase the number of jets [54]. In a typical process, the liquid flows from a reservoir to the edge of the plate, from which multiple jets can be ejected simultaneously.

A co-axial needle was also developed, and it consists of two concentric hollow needles to generate a jet that is coaxially electrified to generate co-axial electrospinning [65], as it is illustrated in Figure 3.12. The co-axial needle can be easily manufactured by inserting a small needle inside a bigger one, in a co-axial configuration. Two syringe bombs are used for both the internal and external needle, at separated flow rates, to direct two fluids. When both the core and shell fluids meet at the end of the co-axial needle, the shell fluid wraps the core fluid to form a Taylor cone in the presence of an external electric field, followed by the ejection of a co-axial jet [56]. After this, nanofibres with different compositions for the core and sheath are obtained, as shown in Figure 3.12.

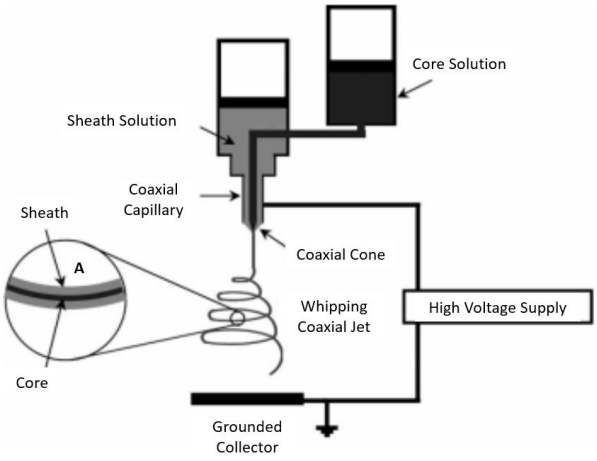

Figure 3.12: Schematic representation of a Coaxial Electrospinning apparatus setup and the resultant fibre. Adapted from [66].

3.3.2 Control of fibre orientation

In order to achieve the highly-aligned nanofibres needed to recreate the mechanical behaviour of cartilage, several techniques have already been used in electrospinning.

A lot of methods for electrospinning rely on changing the collectors. Usually, electrospun nanofibres are deposited on a grounded, solid collector to form a non-woven mat. [56] To have better control of the deposition of the nanofibres, various types of conductive solid collectors, as well as liquid bath collectors, have been stated. Conductive solid collectors can be used in a stationary or dynamic mode. Regarding a stationary collector, it can modulate the distribution of the electric field and, thus, control the orientation of the deposited nanofibres in two different ways: patterning the surface of a conductor substrate with specific structures or combine different substrates with different conductivities to form the pattern [56]. Isolating liquid set in a container below the spinneret has also been demonstrated as a collector. The liquid can act as a coagulation bath to improve the solidification of the jet and produce ultra-thin nanofibres [67].

Conventional Processes for Fibre Orientation

As mentioned previously, there are several types of collectors, such as rotating, parallel, and water bath. Using a rotating collector, such as a wire drum, a wheel, a cone, or a frame in the electrospinning setup, as shown in Figure 3.13, has proven to be the most straightforward and simplest way to fabricate aligned fibres. Matthews *et al.* [68] found that fibre alignment increased with the drum speed, up to a critical level – 12.9 m/s. Additionally, the rotating speed of the collector also affects the diameter of the fibres, the higher the speed, the smaller the diameter [55]. Beachley *et al.* [69] shows that the fibre diameter reduces about 15-40 % with a collector rotating at velocities between 5 to 15 m/s. However, using a rotating collector is extremely time/energy consuming and needs a lot of manipulation.

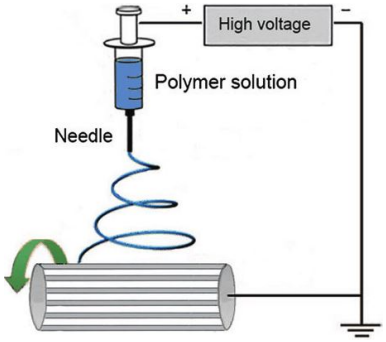

Figure 3.13: Electrospinning setup with rotating collector [50].

Aligned fibres can also be created using a water bath as the collector in electrospinning, as shown in Figure 3.14. Smit *et al.* [70] showed a secure method to collect the fibres by first depositing them in a coagulation bath and then assembling them using a rotating collector. The result was a mesh of electrospun fibres deposited on the surface of the water, which was then attracted to the edge of the bath to be collected by a rotating cylinder. Even though the electrospun fibres were randomly disposed on the water surface, the fibre mesh elongated, and the fibres aligned as the mesh was attracted to the water surface. The surface tension caused the fibre mesh to collapse in a thread when it was lifted from the water surface to the rotary collector, resulting in the collection of aligned fibres [70].

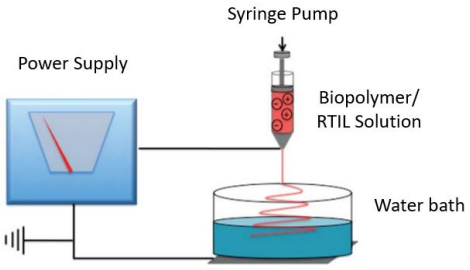

Figure 3.14: Electrospinning setup with a water bath [71].

Another type of collector used is the parallel collector, represented in Figure 3.15a. The parallel collector technique can use electrical forces to induce fibre alignment. Li *et al.* [52] [54] reported a strategy for preparing aligned fibres by using a collector that consists of two pieces of electrically conductive substrates separated by a gap of micrometres, or even centimetres. This insulating gap distance was noted to affect the level of fibre orientation significantly - a more substantial gap could result in better fibre alignment. However, it was observed there was a maximum gap size ($<$ 1 cm for nanofibres thinner than 150 nm) above which the nanofibres would break [56].

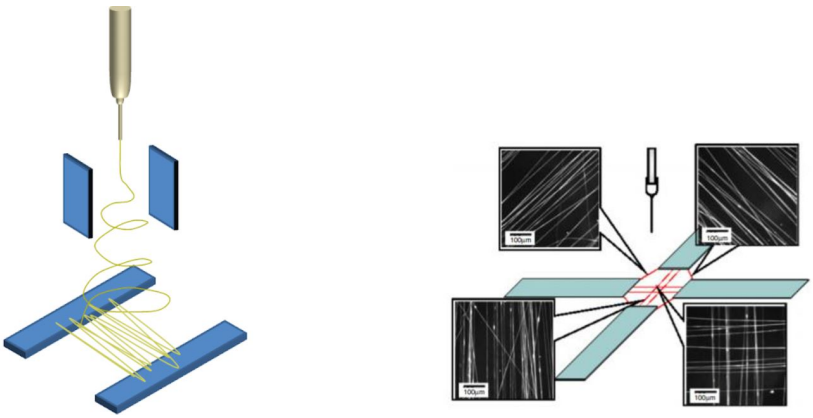

(a) (b)

Figure 3.15: (a) Electrospinning setup with a parallel collector [52]. (b) Electrospinning setup with an array of collector electrodes arranged in parallel [72].

Using a similar concept, Li *et al.* [54] organized an array of collector electrodes arranged in parallel, to create a pattern in the electrospun fibres. However, the pattern formed by the fibres was different in the entire mesh of fibres, and it depended on the

location of the gap, as shown in Figure 3.15b.

Still regarding the method using a gap between the collectors, Dalton *et al.* [73] used two rings placed parallel to each other, at an equal distance from the spinneret, to collect aligned fibres deposited in the perimeter of both rings, as represented in Figure 3.16. Spinning one of the rings, after the fibres were deposited, he managed to obtain a twisted thread with multi-filaments. The apparent result is that the twisted thread has more resistance than the thread constituted only by aligned fibres.

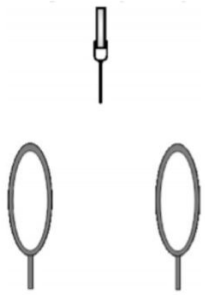

Figure 3.16: Dual ring collector [72].

Using focusing electrodes is another way to control fibre deposition since its main purpose is to restrict the deposition area of the electrospinning jet. The focusing electrode usually comes in the form of a ring, and it is charged with the same polarity as the spinneret tip. Ying *et al.* [74], however, showed that it is also possible to use a non-conducting cylinder. Deitzel *et al.* [75] used several ring electrodes to narrow the fibre deposition area from a diameter of 7 cm to 1 cm. The voltage applied to the ring has to be controlled properly; otherwise, the electrospinning jet will either be repelled or deposit on the ring. The main challenge with using focusing electrodes is to optimize the charges on it so that the electrospinning jet is not repelled from the collector but instead deposits the fibres on specific spots. Huang *et al.* [76] showed that it's possible to narrow down the deposition area to about 0.5 mm using an aluminium-coated shadow mask to narrow the deposited electrospun fibre to a 600 µm diameter area.

The material used was alginate with polyethylene oxide, and the distance between the spinneret tip and the collector was 3 cm. Figure 3.17 shows some schematic representations of configurations that use ring-shaped focusing electrodes.

(a) (b)

Figure 3.17: (a) Controlled deposition using multiple focusing rings [75]. (b) Controlled deposition using only one focusing ring [77].

The alignment of the nanofibres can also be controlled by implementing a magnetic field if the polymer solution contains a small number of magnetic materials. If this is applied, the first force that will be applied to control the alignment of the fibres is the magnetic force. Yang *et al.* [78] designed an auxiliary magnetic field, as shown in Figure 3.18, to fabricate well-aligned fibres and called it Magnetic Electrospinning. In this technique, magnetized nanofibres were stretched into parallel fibres, over an area of more than 5x5 cm, in a magnetic field.

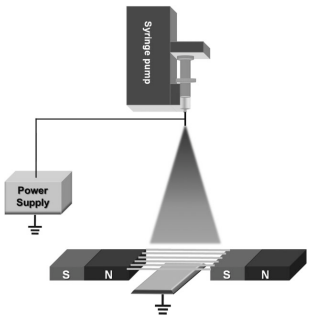

Figure 3.18: Schematic illustration of the setup used in the MES method for preparing aligned nanofibres [79].

Compared with other existing methods to control fibre orientation, magnetic electrospinning has a few advantages, such as the simplicity of both the apparatus and the operation itself, the accuracy on how the magnetic field can be manipulated and the fact that the resultant nanofibres can be transferred onto any substrate from any angles with full retention on their structures, which makes it perfect for constructing more complex 3D designs. However, this method can only be applied for materials with magnetism, and fibres are restricted by a limited length [56].

Teo *et al.* [72] showed the effect a knife-edge electrode has in the deposition of the electrospun fibres, using a configuration as the one shown in Figure 3.19a When the knife-edge electrode was used, instead of conductive tracks, as auxiliary electrodes, the collected fibres showed a much higher level of alignment.

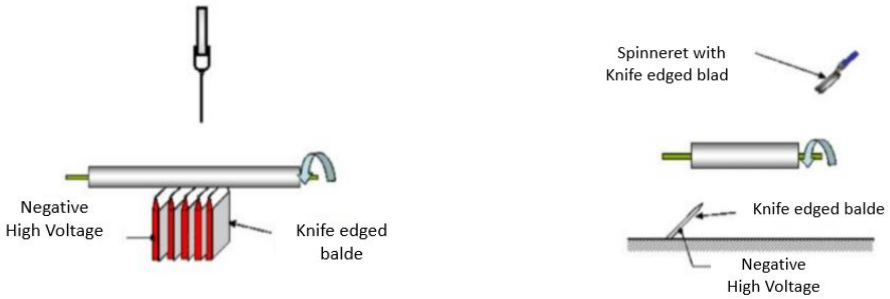

(a) (b)

Figure 3.19: (a) Rotating tube collector with knife-edge electrodes below [72]. (b) Controlling electrospinning jet using knife-edge electrode [72].

Using a similar concept, Teo *et al.* [72] also used a knife-edge electrode to direct the trajectory of the electrospinning jet, as represented in Figure 3.19b. The polymer solution was charged positively, while the electrode was charged negatively so that an attractive force was exerted on the jet. The knife-edge electrode was placed at a certain distance from the spinneret in a way that an angle between the tip of the spinneret and the electrode was created. The result was diagonally aligned fibres.

3.3.3 Database of Patents for Fibre Alignment

Electrospinning Apparatus For Producing Nanofibers

Name: Electrospinning Apparatus For Producing Nanofibers

Inventors: Katti Dhirendra S.; Nandan Amit; Singhal Riju Mohan

Pub. No.: US 2009/0091065 A1

Pub. Date: April 9th, 2009

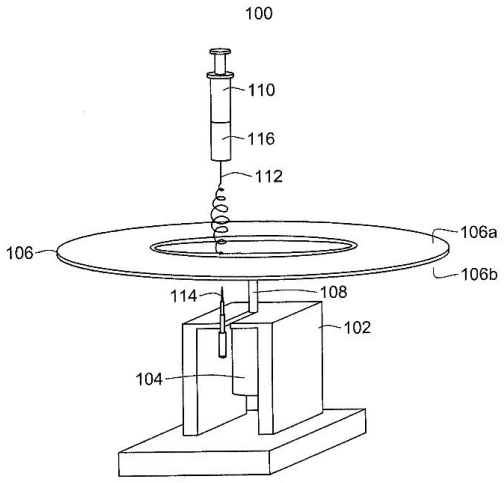

Figure 3.20: Schematic representation of an Electrospinning apparatus for synthesizing aligned and cross polymeric nanofibres. [80]

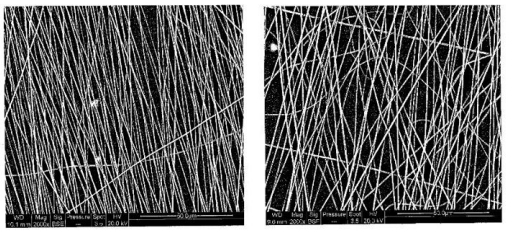

Figure 3.21: Scanning Electron Micrographs of nanofibres obtained using 15% polystyrene (PS) solution taken at different radial distances on the circulating disc surface (9 cm and 13 cm) while rotating the disc at 1500 rpm. [80]

The present patent is of an electrospinning apparatus for producing aligned and crossed nanofibres, represented in Figure 3.20, and the method used. The electrospinning apparatus includes a supporting horizontal surface (106), a DC motor placed below the flat surface (104), a circular rotating disc attached to the DC motor (108), a reservoir with the spinneret (100) placed perpendicularly above the disc surface (106a), and a focusing device (114) that is positioned exactly below the spinneret. The latter is configured to focus the electrospun nanofibres by manipulating the electric field and the disc surface, in order to deposit the nanofibres into a defined region on the disc [80]. The electrospinning spinneret and the focusing device are connected to the opposite terminals of an external high voltage power supply. In Figure 3.21, there are a couple of examples of the results achieved.

Electrostatic spinning orientation fibre preparation device

Name: Electrostatic spinning orientation fibre preparation device

Inventors: Chen Hongbo; Ding Yumei; Li Haoyi; Wu Weifeng; Yang Weimin

Pub. No.: CN 104141174 A

Pub. Date: November 12th, 2014

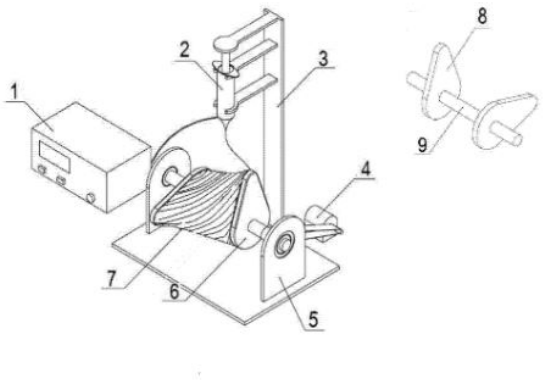

Figure 3.22: Schematic view showing the structure of an apparatus for preparing an electrospun oriented fibre according to the present invention. [81]

The invention provides an electrospinning-oriented fibre preparation device, as shown in Figure 3.22. The main components thereof are an electrospinning nozzle (2), a receiving cam group (6), an electrostatic generator (1), a motor (4), a control system (3) and a bracket (5). The control system fixes the electrospinning nozzle and determines its position [81]. The bracket supports the receiving cam group. The high-voltage output end of the electrostatic generator is connected to the spinneret; the grounding end of the electrostatic generator is connected to the receiving cam group, which is rotated according to a prescribed program [81].

Apparatus for electrospinning 2D/3D structures of micro/nano-fibrous materials

Name: Apparatus for electrospinning 2D/3D structures of micro/nano-fibrous materials

Inventors: Yousef Mohammadi

Pub. No.: EP 2045375 A1

Pub. Date: October 10th, 2007

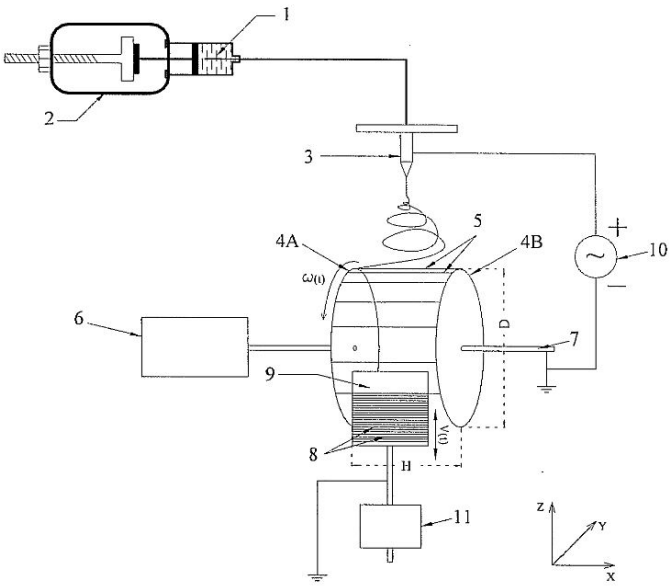

Figure 3.23: Schematic representation of an apparatus method according to a first embodiment of the present invention [82].

Figure 3.23 shows an apparatus for electrospinning capable of precisely controlling both the degree and pattern of the alignment of the micro or nanofibres. Overall, the principle of generating the micro or nanofibres from the solution using the spinneret is comparable to the more common ones so that the detailed description can be overlooked. However, both the alignment mechanism and collection method of the produced fibres are different than the ordinary and will be described below [82]. The nanofibres are aligned between the two-parallel disc-shaped rotating electrodes made of a conductive material. The resulting electrospun fibres are aligned parallelly with each other between the two rotating electrodes [82]. The collector (9) extends substantially perpendicular to the surfaces of the electrodes and is disposed at a radius smaller than the range of the

two electrodes. Thus, the fibres aligned by the electrodes are transported along a circular path and come into contact with the collector. Here they are deposited in a configuration significantly determined by the alignment caused by the rotating electrodes [82].

Electrospinning System and Process for large-scale Manufacturing of Aligned 3D Fibre Matrices

Name: Electrospinning System and Process for large-scale Manufacturing of Aligned 3D Fibre Matrices

Inventors: António Manuel Godinho Completo; Paula Alexandrina de Aguiar Pereira Marques

Pub. No.: EP 3670714 A1

Pub. Date: June 24th, 2020

This is an invention related to the system and process of continuous electrospinning for the production of 3D matrices of aligned polymeric fibres, with application in the medical fields, in tissue engineering. A representative image of the system, and the resulting matrix of fibres, are shown in Figures 3.24 and 3.25, respectively. The system contains a capillary tube (3) with positive polarity, a set of multi-electrodes with negative polarity inserted in a peripheral support (15), having each electrode (7) controlled movement that allows its exposure to the electrospinning tube. It contains also a central collecting table (17) of electrospun fibres, covered in holes (6,16) connected to a chamber and a vacuum pump (13). The 3D aligned matrices of fibre are formed by the deposition of layers (30), when exposing the electrodes to the capillary tube.

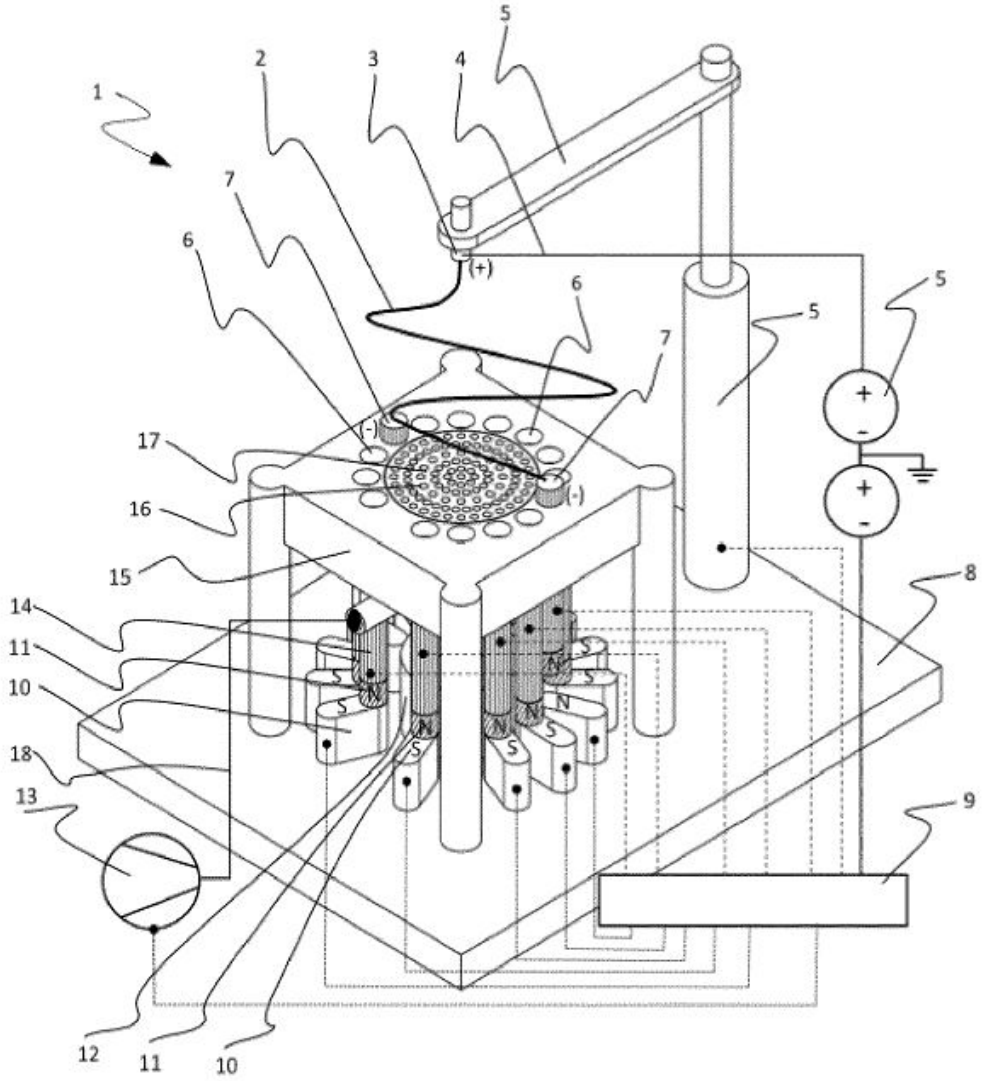

Figure 3.24: Schematic representation of the electrospinning equipment and process to produce 3D matrices of aligned nanofibres.

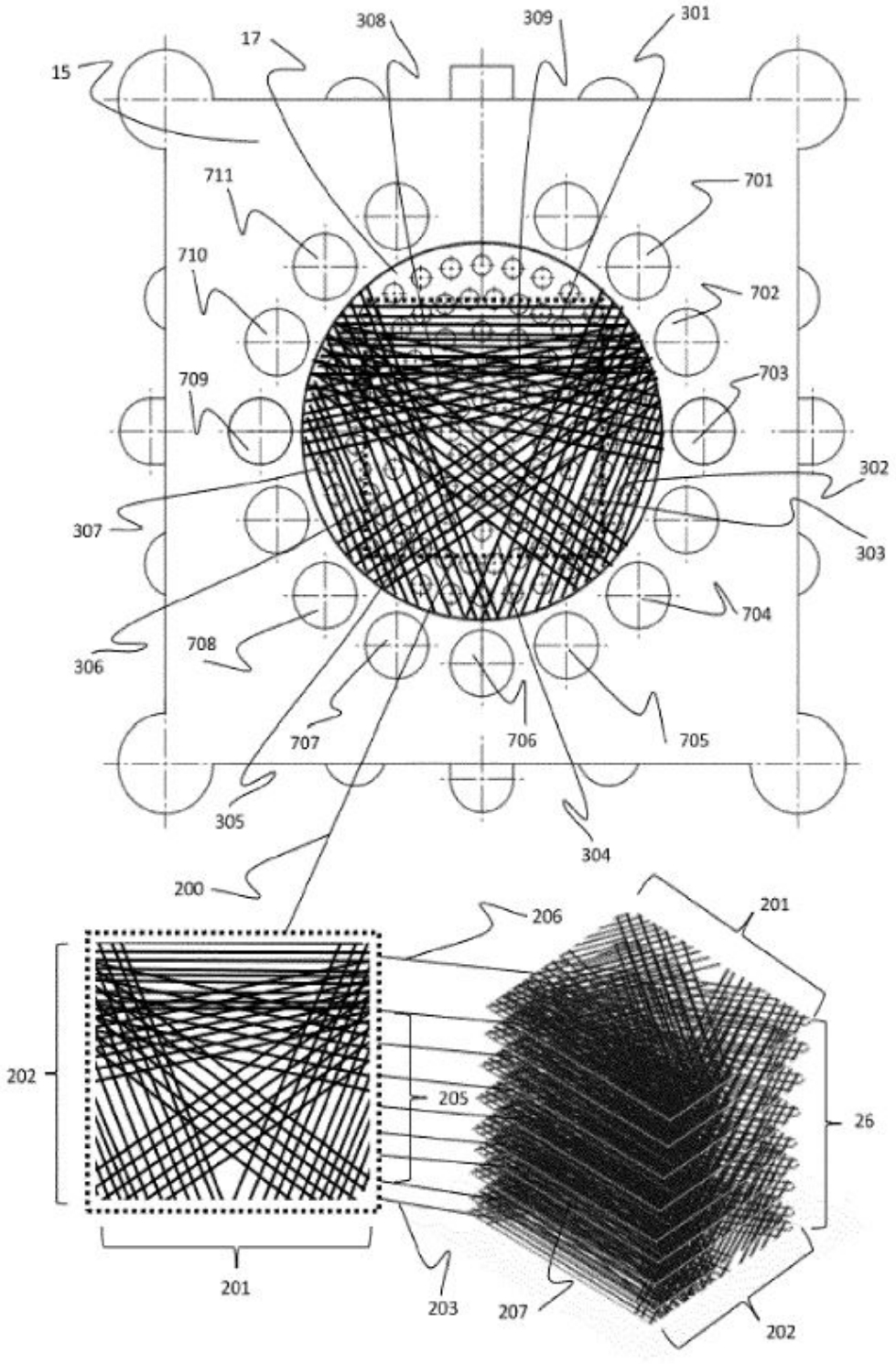

Figure 3.25: Schematic representation of disposal of the layers of the resulting 3D matrix of fibres.

Chapter 4

Electrospinning Experiment Plan

4.1 Introduction

This chapter is relative to the experimental phase of the dissertation. Before conducting the experiments with the electrospinning equipment, it is crucial to have a general idea of how the input parameters will affect the resulting nanofibres' morphology. In the first phase, both the input and the output machine parameters are presented and based on that, design of experiments is developed, using a 2-level factorial design. A Matlab theoretical model to predict the experimental behaviour of the space between the nanofibres is also introduced in this chapter. Further ahead, a statistical analysis of the significance of the input parameters and how much they affect the output results are presented.

4.2 Design of experiments (DOE)

The most effective way to improve product quality and reliability is to integrate them into the design and manufacturing process [83]. A design of experiments is a systematic method used to understand how the process and product parameters affect the response variables. It is a mathematical tool used to define the significance of specific processing and product variables, and how to manage them to optimize the entire system performance. It is a technique adopted by many industries, such as automotive, semiconductor, medical devices, and chemical products, amongst others.

A DoE is useful for a wide range of purposes. It can be used for comparisons between multiple design options, variable screening (to understand which parameters affect the process the most), transfer function exploration, system optimization, and system robustness (to make the system robust against uncontrollable factors) [83].

Most of the current statistical approaches to design experiments originated from the work of R.A. Fisher [84] in the early 20th century. There are various design types, and they are used according to the purposes of the DoE in question, as shown in Table 4.1.

Table 4.1: Purposes of DoE and design types [83].

Purpose of the DoE	**Design type**
Comparison	One factor design
Variable screening	2 level factorial design Taguchi orthogonal array Plackett-Burman design
Transfer function identification & optimization	Central composite design Box-Behnken design
System robustness	Taguchi robust design

In the context of this dissertation, since the primary purpose of the use of the DoE is to understand how the different electrospinning parameters affect the deposited nanofibres and which are more relevant, a 2 level factorial design or a Taguchi orthogonal array design are the most suitable.

When creating a DoE, there are a few important concepts to take into consideration, such as blocking, randomization, and replication. Randomizations is related to the order in which the trials are performed, which allows eliminating the effects of uncontrollable variables. Blocking is used when randomizing a factor is impossible; it will enable the restriction of the randomization by carrying out the trials with one set of the factor, and then all the tests with the other set. Replication is the repetition of a complete experiment treatment, including the setup [85].

4.3 Establishment of an Experiment Plan for Fibre Electrospinning

4.3.1 Introduction

The purpose of the DoE, as mentioned previously, is to understand how and/or if the input parameters have a significant impact on the output results. The electrospinning equipment in question, as it will be detailed explained further ahead, has an emitter module, a collecting module, and a deposition module. Since the goal of this dissertation is to understand if the fibre's disposition can be controlled in order to recreate the cartilage's fibrillar organisation, the main focus will be on finding out whether the collecting and deposition module will have a significant impact on the resulting nanofibres' disposal.

The first step is then understanding which parameters to take into consideration and deciding which output variables are worth measuring for further analysis of the results. After this, the DoE is adequately designed, and a set of experiments are conducted having it as a base.

4.3.2 Input and Output Variables

In general, several factors can influence the electrospinning process; this is what makes its optimization process such a complex one. Table 4.2 shows the parameters that have been studied, as well as optimized, over the years as the ones that have the most influence on the process.

The electrospinning equipment used for this dissertation, as mentioned previously, is constituted by three modules: emitter, collecting and deposition module. The collecting module is no less than two parallel rotating bands, as schematically represented in Figure 4.1a. The gap between the bands is big enough to allow the deposition table to collect a fraction of the fibres that are attracted to the bands. The deposition table has both linear and rotational movement, as schematically represented in Figure 4.1b.

Table 4.2: Parameters affecting the electrospinning process, in general [86].

Parameter	Description
Polymer properties	Molecular weight Solubility
Polymer solution parameters	Concentration Viscosity Conductivity Surface Tension pH
Process conditions	Distance Applied voltage Flow rate Polarity of the needle Needle diameter
Ambient parameters	Humidity Pressure Temperature

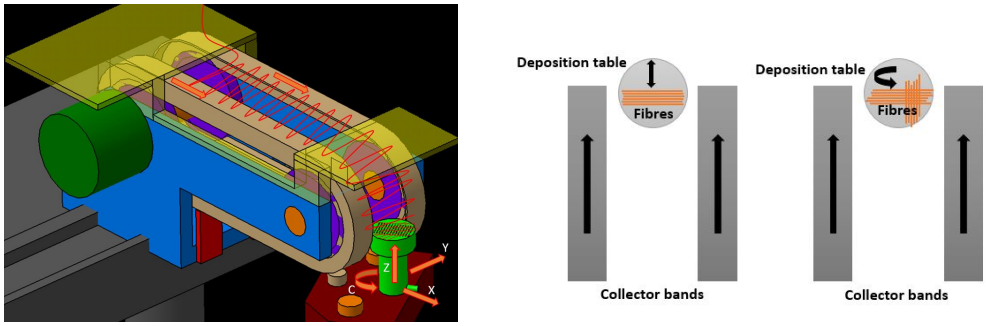

(a) (b)

Figure 4.1: (a) CAD visualization of the collecting bands design and the deposition table, as well as representation of the movements performed by each component. (b) Schematic representation of the principles of the deposition table. Adapted from [87]).

Having a better understanding of how the electrospinning equipment's modules work, it is easier to make a prediction on which factors could have a direct effect on the space between the fibres. The velocity of the collecting bands, as well as the velocity of the deposition table, are the two factors that stand out for the ease of control they provide. Moreover, the flow rate is also a defining factor on the space between the fibres since it controls the amount of fibre that leaves the syringe. For better visualization, the input

parameters taken into consideration are stated in Table 4.3, as well as the maximum and minimum values used for each factor.

Table 4.3: Electrospinning input parameters and interval of values for each factor.

Parameter	**Factor**	**Low-High**	**Coded**	
			Low	High
Velocity of the collector bands	A	1000-6000 mm/min	-1	1
Velocity of the deposition table	B	125-750 mm/min	-1	1
Flow rate	C	1,5-4 mL/h	-1	1

The output variables to be evaluated will be the space between the fibres since the main goal of the dissertation is to understand how this variable is affected in order to find an effective way to produce highly aligned fibres. The second output variable to be screened is the size of the pores, which is highly dependent on the previous variable mentioned. Finally, the third output variable will be the diameter of the resulting fibre. The space between the fibres is the main factor to be analysed through the dissertation because it is highly connected with the size of the pores of the resulting fibre matrix. The pore size is a critical factor for the chondrocytes' migration progress into the 3D construction.

4.3.3 Creation of the DoE

Once the input and output parameters are defined, it is possible to construct the design of experiments. As mentioned previously, in Section 4.2, a 2-level factorial design is the more fitted for this problem. Since there are three factors, 2^3 experiments need to be conducted; however, to reach more accurate results and to analyse interactions between elements, replication will be used. The full DoE matrix is represented in Table 4.4, with a total of 16 experiments. The parameter's high and low values, described in Table 4.3, were defined based on previous experiments realised in other studies, such that the difference between the "high" and "low" levels would most likely have a statistical impact. There is, however, a chance that not all the trials will create continuous fibres due to new parameter settings that were not tested beforehand.

Table 4.4: Design of Experiments Table.

	Factors			**Interactions between factors**				**Experimental Parameter Values**		
Experiment	A	B	C	AB	AC	BC	ABC	A	B	C
1	-1	-1	-1	1	1	1	-1	2000	250	2
2	1	-1	-1	-1	-1	1	1	6000	250	2
3	-1	1	-1	-1	1	-1	1	1000	500	2
4	1	1	-1	1	-1	-1	-1	6000	500	2
5	-1	-1	1	1	-1	-1	1	1000	125	3
6	1	-1	1	-1	1	-1	-1	4000	250	3
7	-1	1	1	-1	-1	1	-1	2000	500	3
8	1	1	1	1	1	1	1	6000	500	3
9	-1	-1	-1	1	1	1	-1	1000	500	2
10	1	-1	-1	-1	-1	1	1	5000	500	1,5
11	-1	1	-1	-1	1	-1	1	3000	750	1,5
12	1	1	-1	1	-1	-1	-1	4000	750	1,5
13	-1	-1	1	1	-1	-1	1	2000	500	4
14	1	-1	1	-1	1	-1	-1	4000	500	4
15	-1	1	1	-1	-1	1	-1	3000	750	4
16	1	1	1	1	1	1	1	5000	750	4

4.4 Matlab routine to simulate Fibre Alignment

4.4.1 Introduction

Theoretically analysing the entire process, it is easy to have a general idea of the output results, if no errors or outside factors were influencing. Thus, following some theoretical assumptions it was created an objective function, taking into account the variables of the process - flow rate, the velocity of the collecting bands, and velocity of the deposition table -, which defines the behaviour of the fibres when it comes to the space formed between them. This is important because if there is an effective way to predict the space between the electrospun nanofibres, it becomes an easier task to plan the experimental trials. Moreover, understanding how the electrospinning process responds to the change of the input parameters would be of great help to achieve the goal of recreating the fibrillar organisation of the cartilage's native tissue.

4.4.2 Materials and Methods

The theoretical model was based on some conceptual assumptions, and knowledge, on how the equipment works. The premises taken into consideration were the following:

- Taking both the flow rate (F) and the velocity of the collector bands (V_{bands}) as constants, the distance between the deposited fibres **on the deposition table** will increase with the increase of the velocity of the deposition table (V_{table}).
- The velocity of the collecting bands (V_{bands}) should not have an effect on the space between the fibres **on the deposition table**, however, it should affect the fibre spacing on the collecting bands.
- Taking both the velocity of the collector bands (V_{bands}) and the velocity of the deposition table (V_{table}) as constants, the distance between the deposited fibres will decrease with the increasing of the flow rate (F).

Consider that the polymer used on the experiment is released from the syringe at a constant velocity, calculated as shown in Equation 4.1.

$$V_{Fibre} = \frac{F}{\pi \cdot r_{needle}^2} \qquad [mm/min] \tag{4.1}$$

The collecting bands have a width of 12 mm each, as well as the gap distance between them. Thus, the total width (W) available for the deposition is 36 mm. Considering now that the velocity of the collecting bands is zero, the time it takes to deposit a thread of fibre ($t_{deposition}$) can be calculated by Equation 4.2.

$$t_{deposition} = \frac{W}{V_{Fibre}} \qquad [min] \tag{4.2}$$

Having the time each segment of fibre takes to be deposited on the collecting bands, it is possible to calculate the space between the fibres on the collecting bands ($Space_{bands}$) by multiplying the time of deposition with the velocity of the collecting bands (V_{bands}), as shown in Equation 4.3.

$$Space_{bands} = V_{bands} \cdot t_{deposition} \qquad [mm] \tag{4.3}$$

In order to calculate the space between the deposited fibres on the deposition table, since its velocity is a parameter that can be controlled, a simple multiplication of the latter by the time it takes to deposit the fibres on the collecting bands should result in the space between the fibres on the deposition table - Equation 4.4. This is in accordance with the theoretical assumptions presented previously. The velocity of the collecting bands will not affect the space between the deposited nanofibres on the deposition table, and increasing the velocity of the deposition table will increase it.

$$Space_{table} = \frac{Space_{bands}}{V_{bands}} \cdot V_{table} \qquad [mm] \tag{4.4}$$

4.4.3 Preliminary Results

This theoretical model was tested in Matlab in order to see if it is functional and if it can predict the behaviour of the resulting space between the fibres. For an analysis on how each variable affects the result maintaining the other parameters constant, it was conducted a graphical interpretation of the problem, represented in Figure 4.2. The graphs show that the velocity of the collecting bands doesn't have any effect on the space between the fibres collected by the deposition table. This makes sense due to the fact that when the fibres are on the collecting bands, the only factor that should affect the space they will have on the deposition table is the velocity of the latter. The faster the table moves the fewer fibres it collects, thus, the bigger the space between them.

Prior to the testing with the values from the design of experiments, a few runs were conducted with random values associated with each parameter, in a Matlab routine, to have a visual understanding on the general behaviour of the function. Figure 4.3 shows the prediction of the theoretical model for two sets of random values. The values of each parameter are presented in Tables A.4 and A.5 in Appendix A. Analysing the values used for the settings in each trial it can be confirmed that the model can, in fact, make a general prediction on whether the space between the fibres will increase, decrease or keep constant for each experiment.

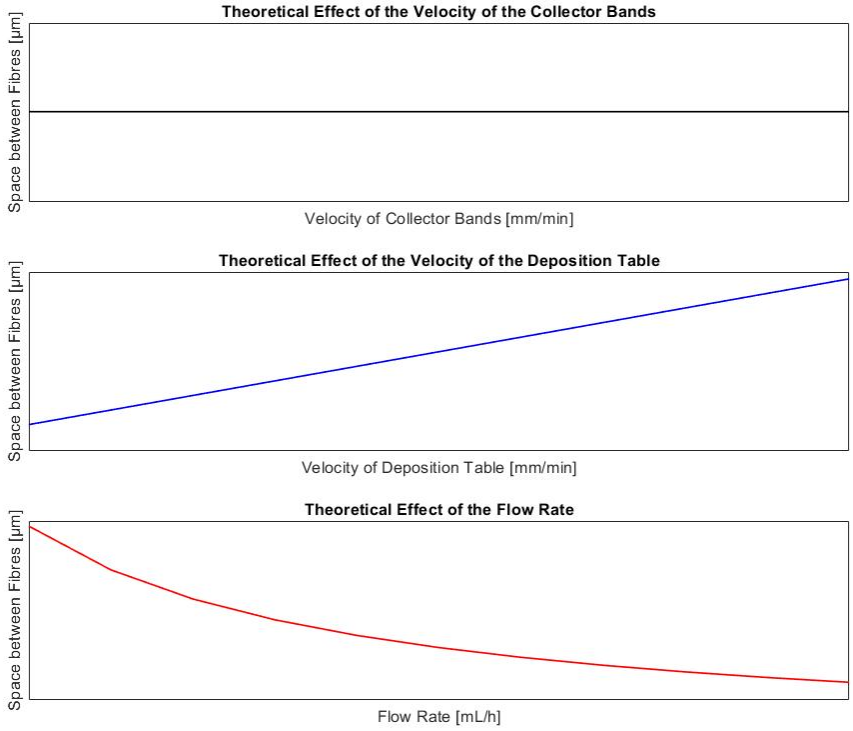

Figure 4.2: Theoretical model's response to variations on the input variables.

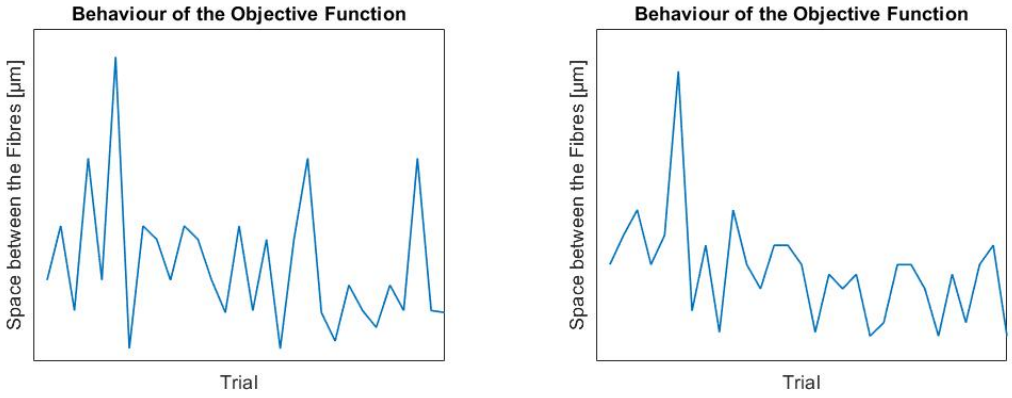

(a) (b)

Figure 4.3: Theoretical Model's prediction for two sets of 30 random experiments - (a) and (b).

The previous trials aren't enough to understand how good the theoretical model is, it is necessary to account the error percentage between the values predicted by the model and the real experimental values. In order to do that, a theoretical prediction with

the values from the design of experiments was conducted, which will then be compared with the experimental trial's results. The theoretical model's prediction is represented in Figure 4.4.

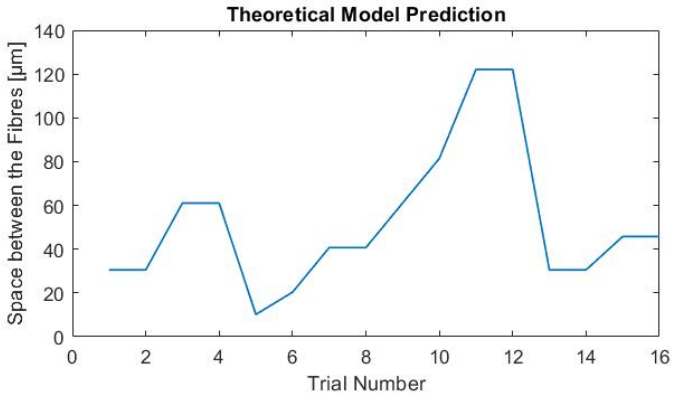

Figure 4.4: Prediction of the experimental results variation based on the theoretical model.

4.5 Experimental trials based on DoE

4.5.1 Materials e methods

The Electrospinning equipment used to conduct the experiments is the one represented in Figure 4.5, with both the safety door closed (left) and opened (right).

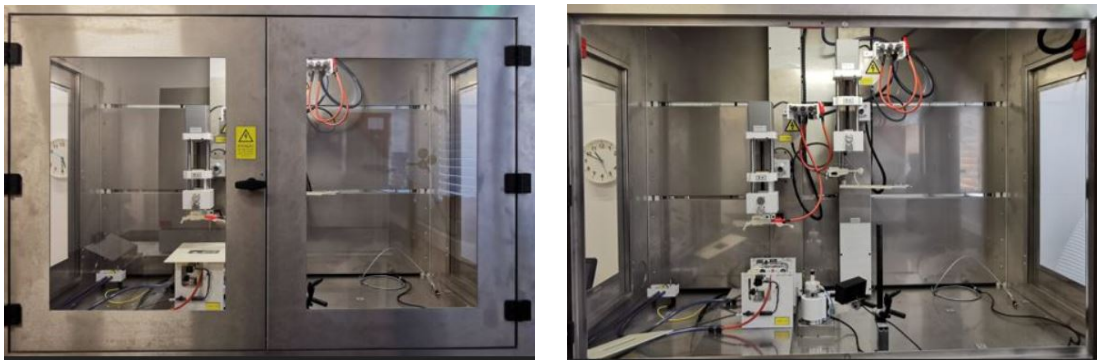

(a) (b)

Figure 4.5: Electrospinning Equipment installed in Centre for Mechanical Technology and Automation - TEMA - with door closed (a) and with door opened (b).

Throughout the entire experimental procedure, the solution used to conduct the experiments was Polycaprolactone(PCL)/Gelatin, mixed in a solvent of Trifluoroethanol

(TFE). Previous studies showed that PCL mixtures are the best to form aligned nanofibres and to recreate cartilage's composition. PCL is a biodegradable polymer approved for biomedical applications by the U.S. Food and Drug Administration (FDA). It is extensively used in plenty of biomedical studies due to the suitable tensile property and biocompatibility [88]. However, this polymer's hydrophobicity and slow biodegradation rate are restraints on its applications. Gelatin is a congener protein of collagen and is a widely utilized biomaterial [89]. However, its fast degradation time and its highly hydrophilic surface may not be appropriate as the base material. In order to overcome the respective defects of these two materials and take each other's advantages, the PCL/gelatin hybrid nanofibre structure has been acquired from electrospinning and been successfully used in biomedical application [90].

The solution was placed inside a syringe attached to a pump, which forms the emitter module of the equipment, as it can be seen in Figure 4.6. The syringe's needle was placed at 15 cm from the collector bands; however, this distance can be adjusted as the operator wishes. Besides the emitter module, the equipment also contains a collecting and deposition module. The collecting module, also shown in Figure 4.6, and as mentioned previously, consists of two rotating, metallic bands, that attract the electrospun fibres. The result is a fibre mat formed in the gap existing between the two bands, as shown in Figure 4.6, to the right. It is essential to mention that the rotating bands are placed above any other component, so the fibres don't end up retained on different surfaces, and, in order to attract the electrospun fibres, and posteriorly align them, the bands are the only metallic component in the module.

The moving table then collects a specific ratio of the resulting mat of fibres. The deposition table moves linearly along the three-axis (XYZ), and rotates around the Z-axis (C), as schematically explained in Figure 4.7. The resulting deposited fibres on the table, look like the example also shown in Figure 4.7, to the right.

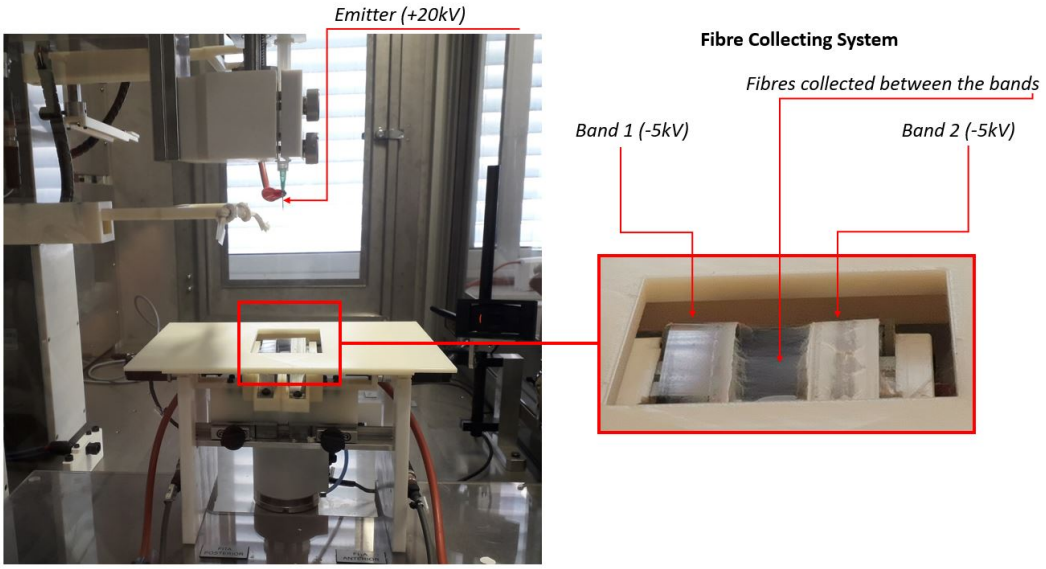

Figure 4.6: Electrospinning setup and its fibre collecting system.

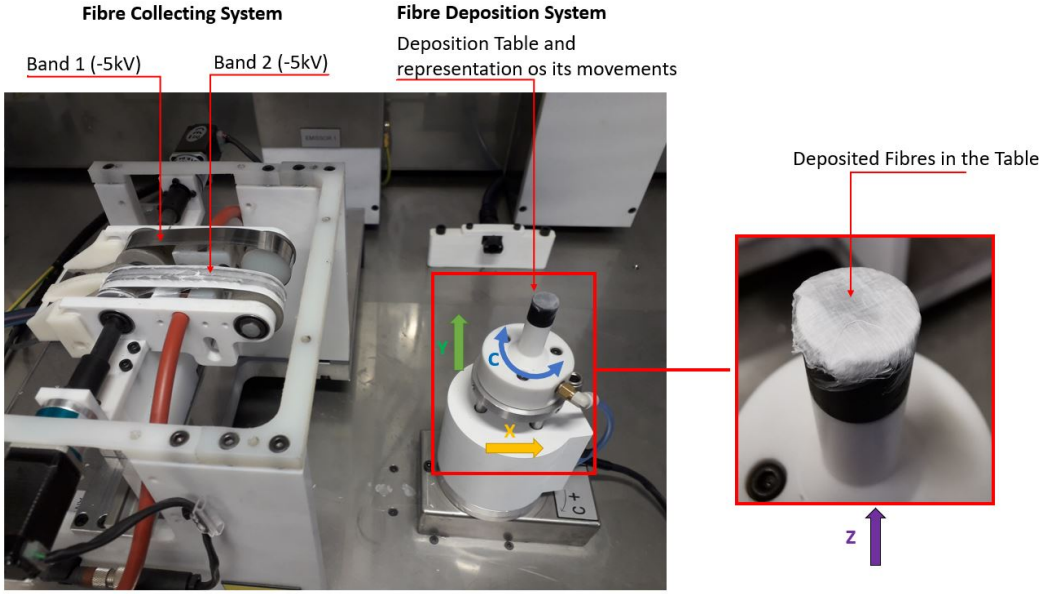

Figure 4.7: Electrospinning setup and its fibre collecting system.

A CNC (Computer Numeric Control) program was developed to control the various movements of the components of the electrospinning equipment. With numeric control, it is possible to control the positioning movements of a mechanical element, in which the commands of that specific movement can be automatically elaborated through digital pieces of information, manually set or through a particular program. The software developed for the electrospinning equipment has both a manual and an automatic mode. Initially, in manual mode, all the components are pre-positioned for a better elapsing of the experiments. The syringe pump position is adjusted, as well as the deposition table, which is set to work zero. After defining the initial positions, the desired CNC routine can be programmed in the Program window. Here, the operator can determine the parameter values (velocity of the collector bands, the velocity of the deposition table and flow rate), the final position, the amount of rotation of the deposition table, and the number of cycles. The program is saved and can be run in automatic mode. The three windows of the software are shown in Figures 4.8, 4.9, and 4.10.

In total were conducted twenty-four experiments; however, since the design of experiments considers only sixteen trials, those are the ones relevant for the analysis. It is essential to mention that, for each test, five cycles were made, i.e., each sample has five layers for each alternating orientation of the deposition table - 0°and 90°. After finishing conducting the experiments, the dry electrospun samples were submitted to a scanning electron microscopy (SEM) present in the Centre for Mechanical Technology and Automation (Hitachi-TM4000Plus). In subsection 4.5.2 are presented the sample results of the sixteen experimental tests, as well as the SEM images at two different scales for better visualisation. In order to obtain the measurements of the fibre diameter, the pore sizes, and the spacing between the fibres, it was used the free software - ImageJ. The results are displayed in the next subsection.

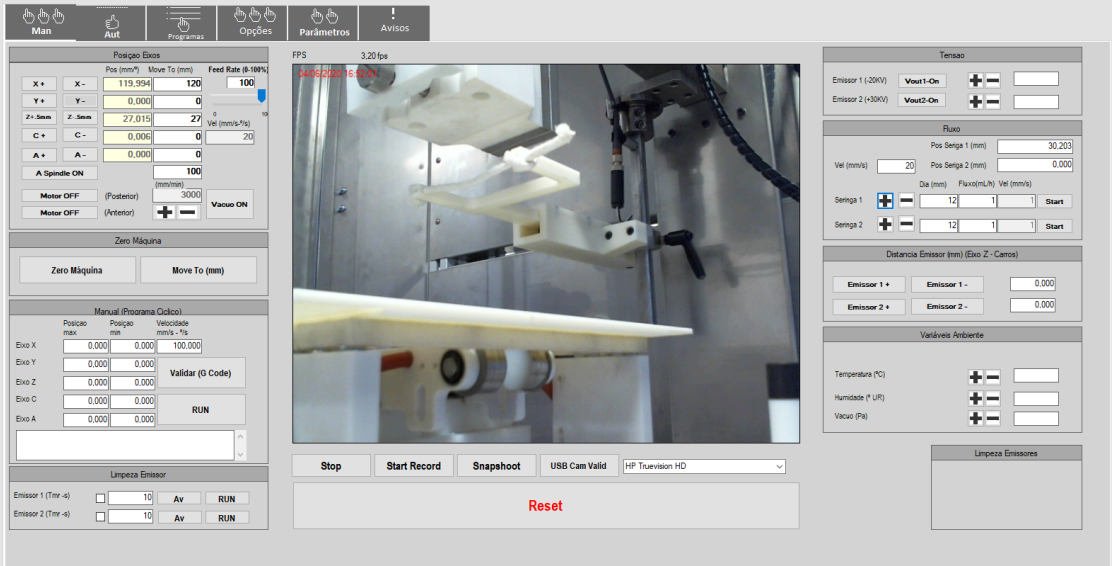

Figure 4.8: Manual Mode of the software developed for the electrospinning equipment.

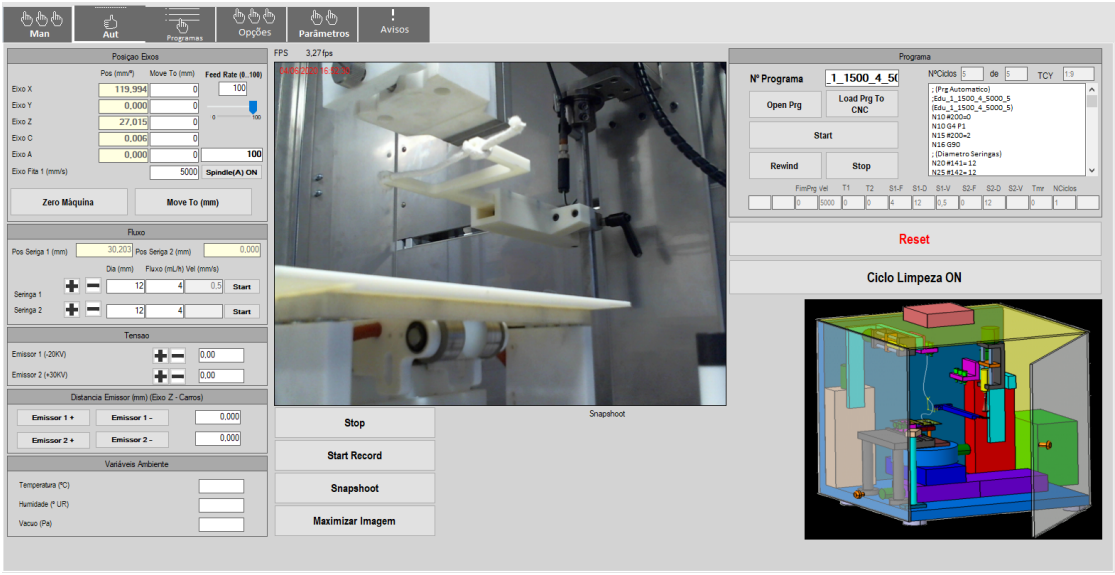

Figure 4.9: Automatic Mode of the software developed for the electrospinning equipment.

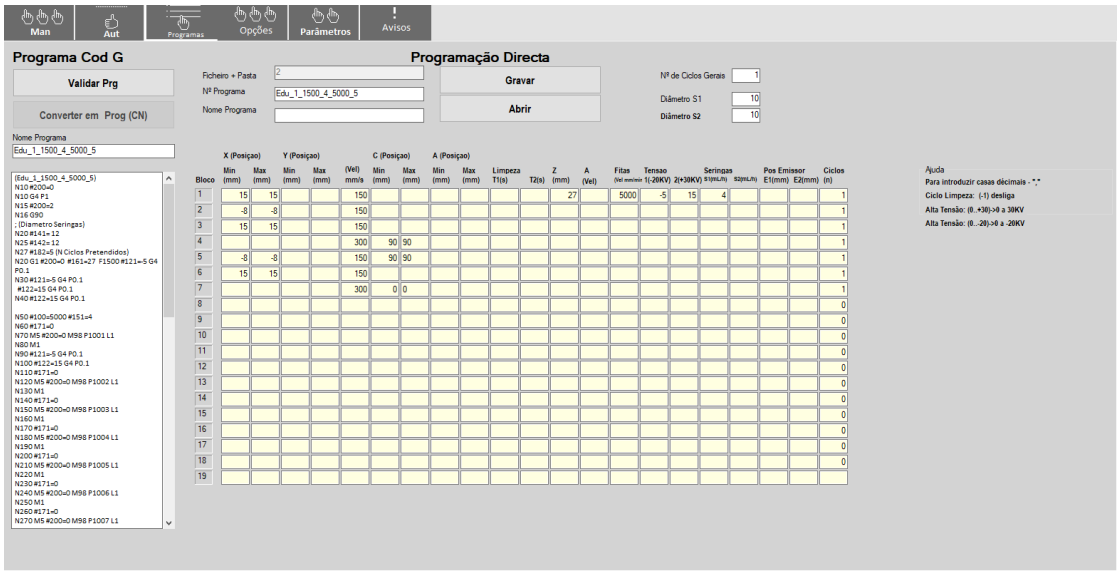

Figure 4.10: Programming Window of the software developed for the electrospinning equipment.

4.5.2 Results

This subsection contains the experimental results and their analysis. For a better contextualization of the experimental work that was realized, a set of images of the sample fibres for each experiment, and its own SEM visualization, are presented. Two SEM images are shown for each experimental trial, at different scales, for a better display of the fibre orientation and spacing.

Sample Results and SEM Images

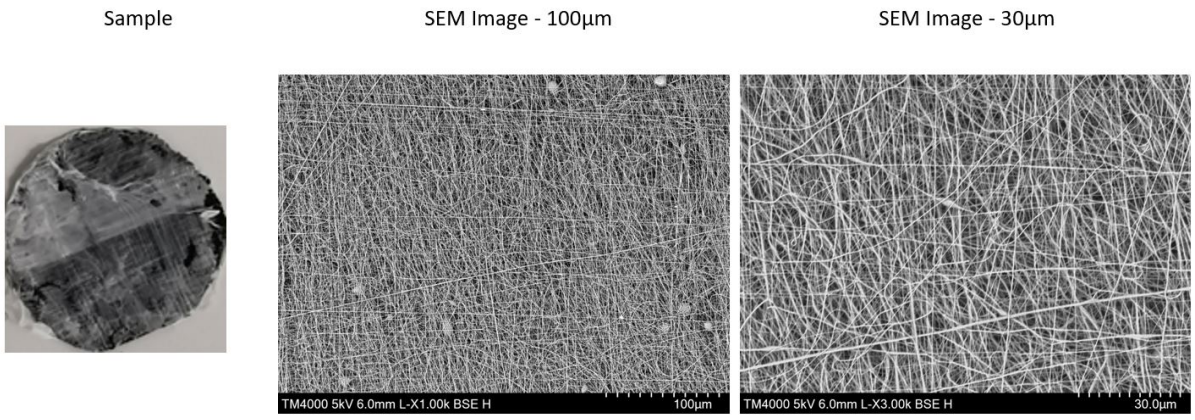

Figure 4.11: Sample 15 (trial nº1) and referent SEM image at two different scales.

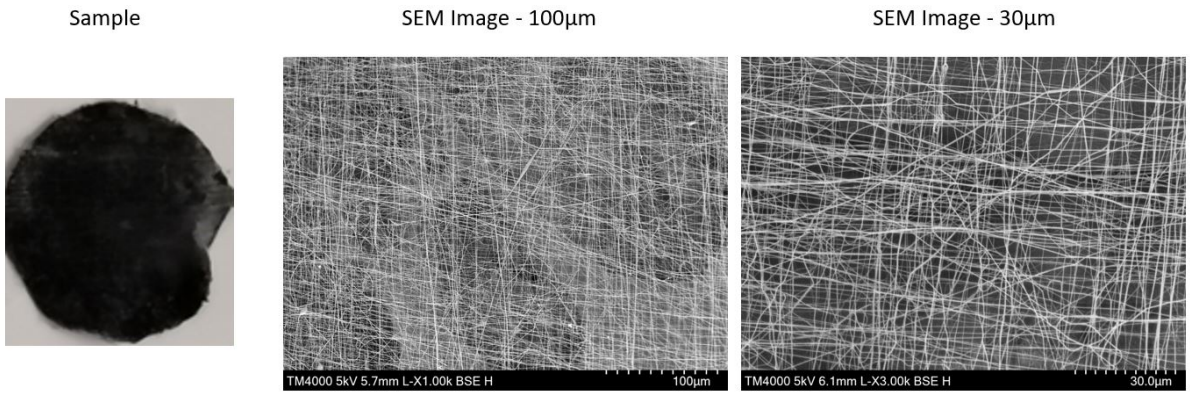

Figure 4.12: Sample 10 (trial nº2) and referent SEM image at two different scales.

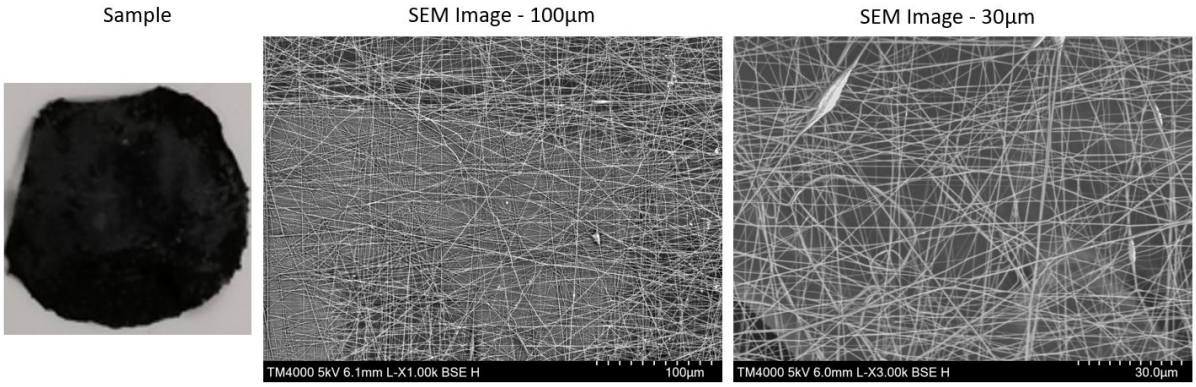

Figure 4.13: Sample 2 (trial nº3) and referent SEM image at two different scales.

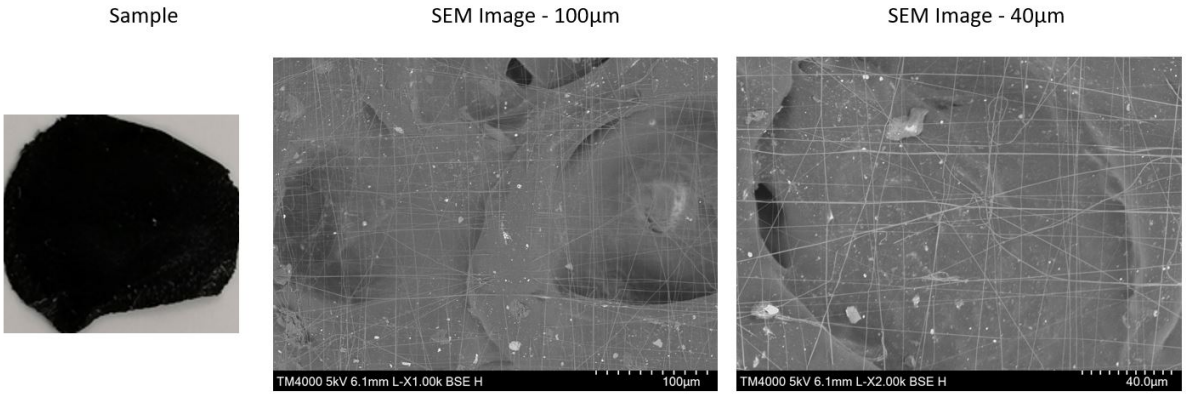

Figure 4.14: Sample 11 (trial nº4) and referent SEM image at two different scales.

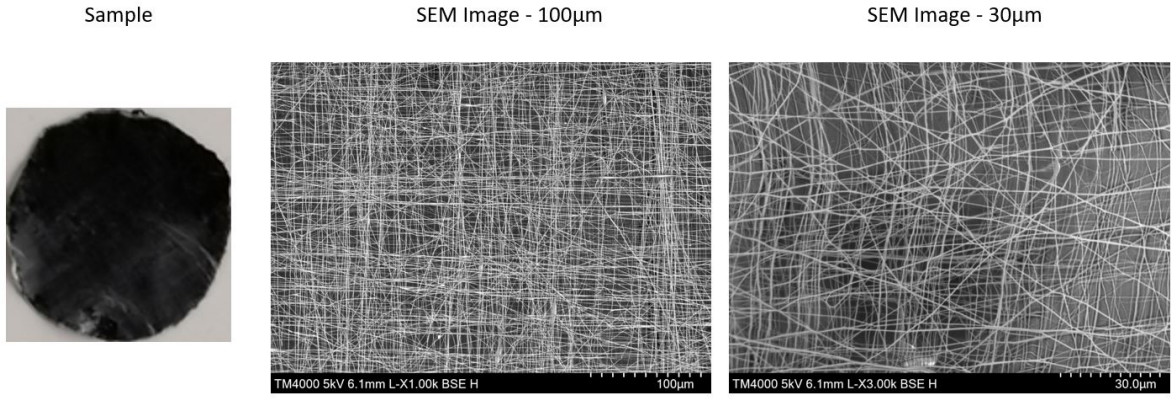

Figure 4.15: Sample 7 (trial nº5) and referent SEM image at two different scales.

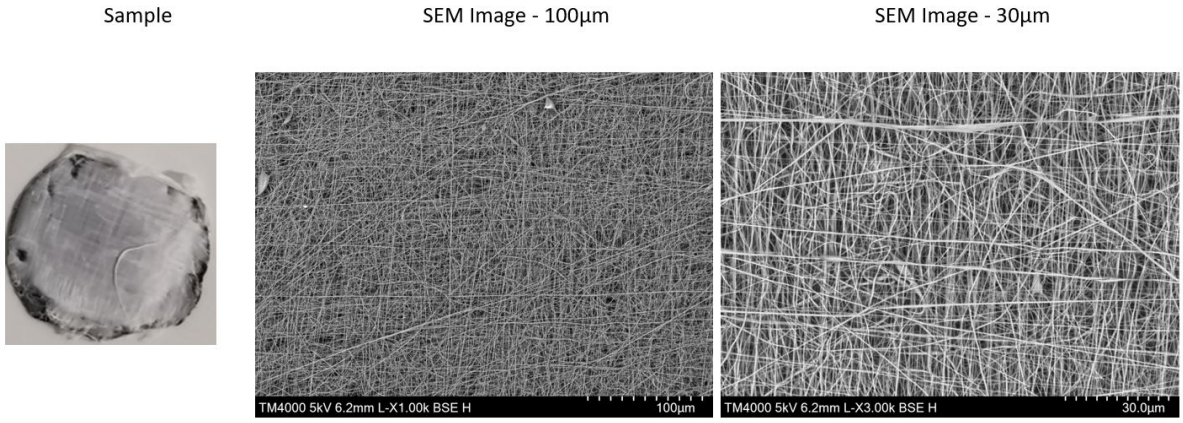

Figure 4.16: Sample 16 (trial nº6) and referent SEM image at two different scales.

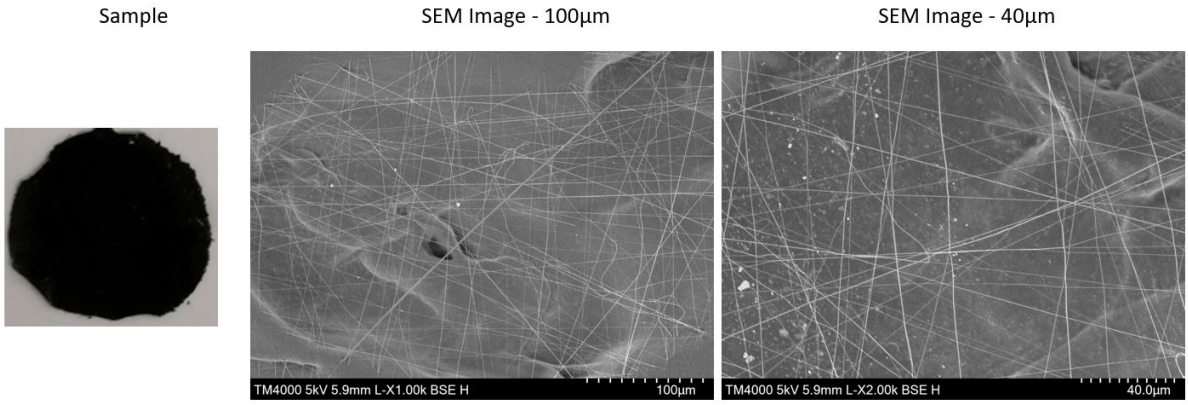

Figure 4.17: Sample 14 (trial nº7) and referent SEM image at two different scales.

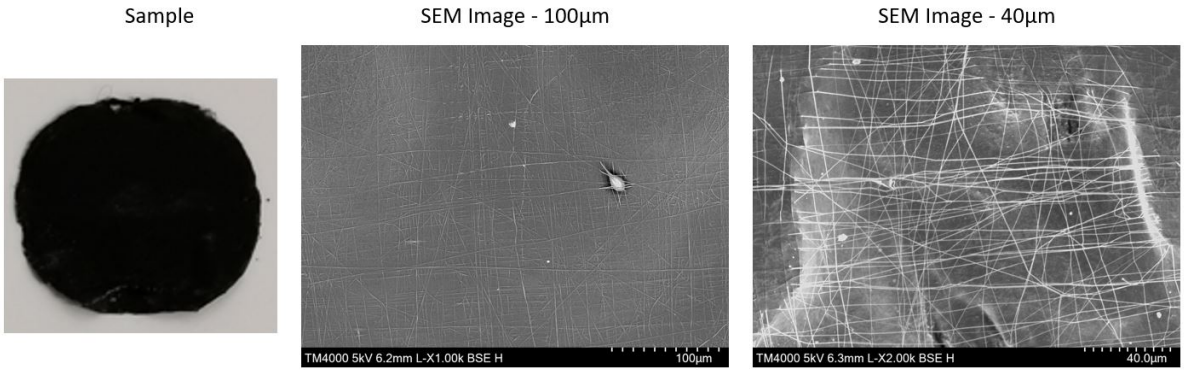

Figure 4.18: Sample 5 (trial nº8) and referent SEM image at two different scales.

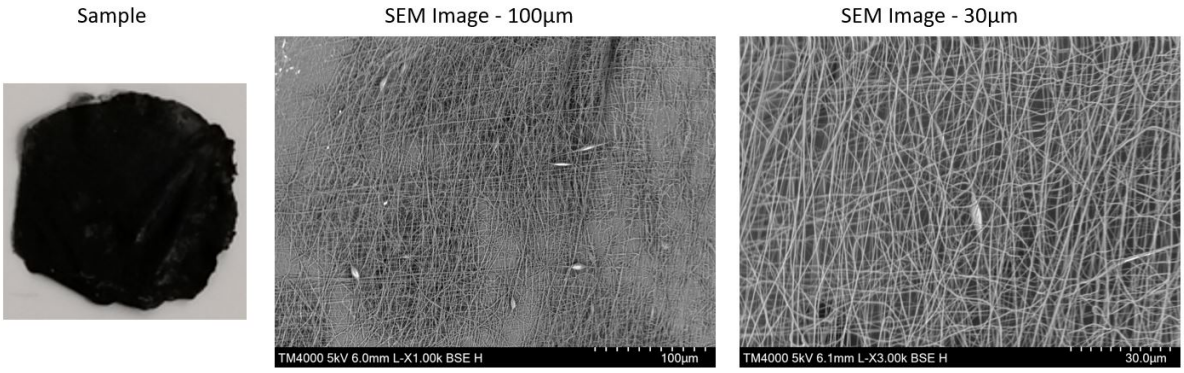

Figure 4.19: Sample 3 (trial nº9) and referent SEM image at two different scales.

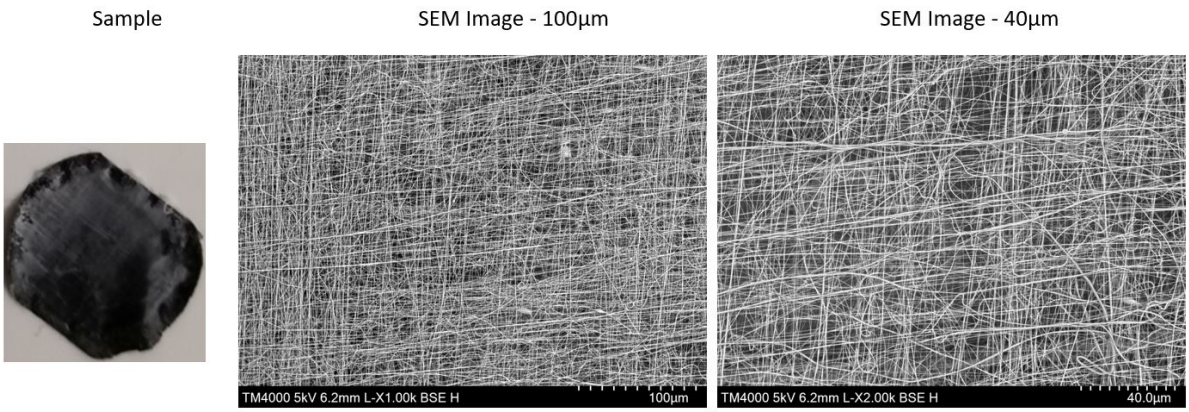

Figure 4.20: Sample 23 (trial nº10) and referent SEM image at two different scales.

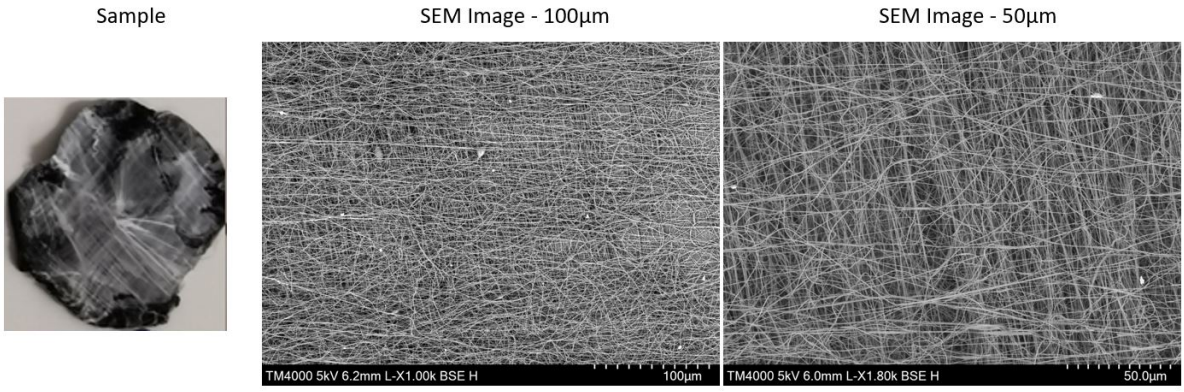

Figure 4.21: Sample 19 (trial nº11) and referent SEM image at two different scales.

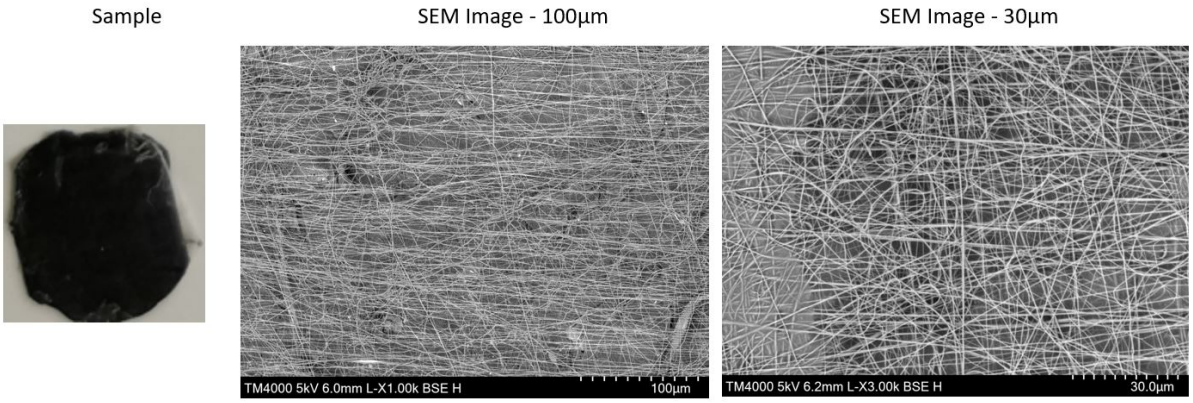

Figure 4.22: Sample 20 (trial nº12) and referent SEM image at two different scales.

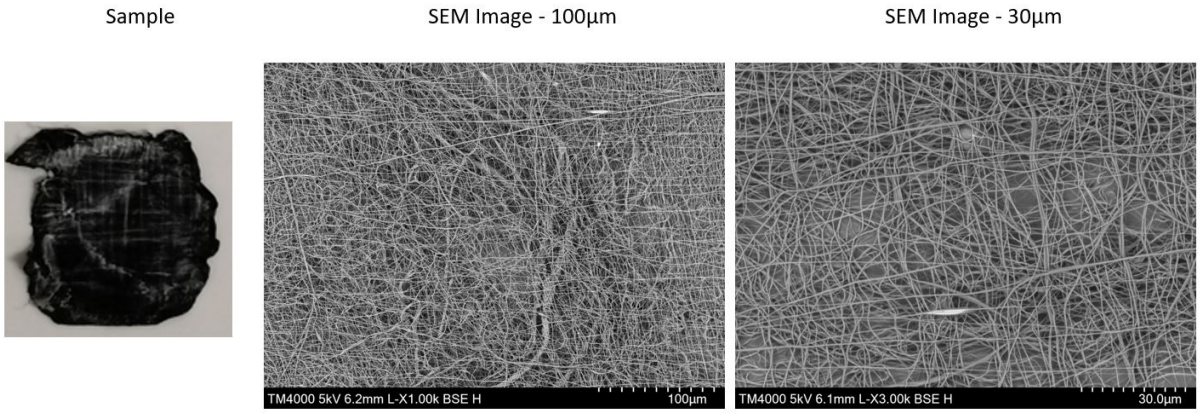

Figure 4.23: Sample 17 (trial nº13) and referent SEM image at two different scales.

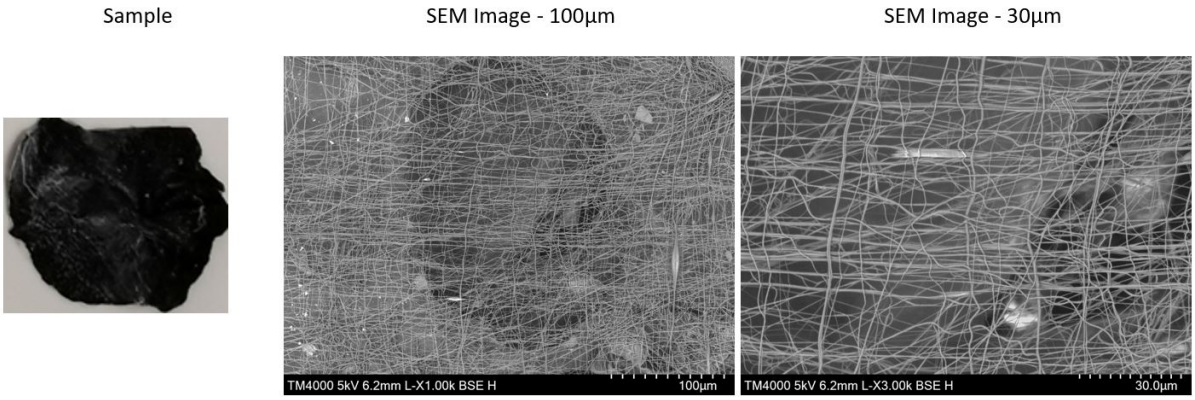

Figure 4.24: Sample 18 (trial nº14) and referent SEM image at two different scales.

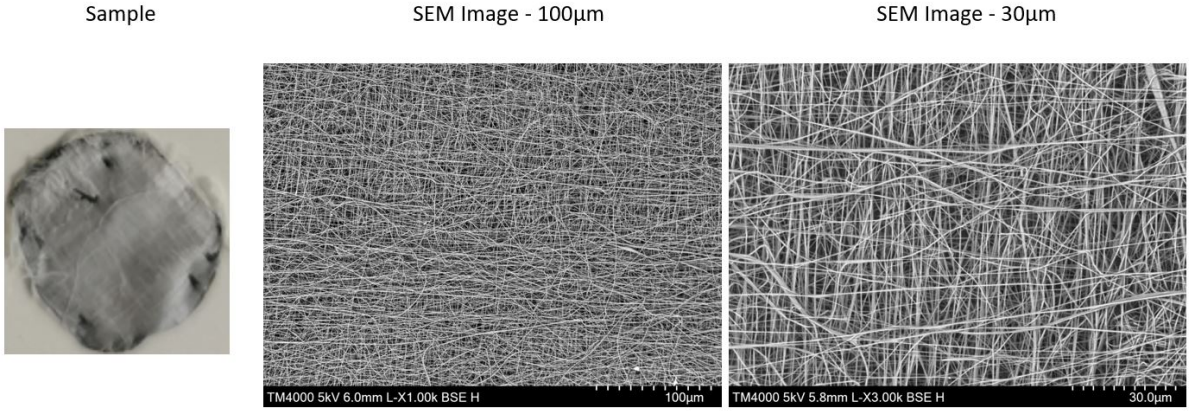

Figure 4.25: Sample 21 (trial º15) and referent SEM image at two different scales.

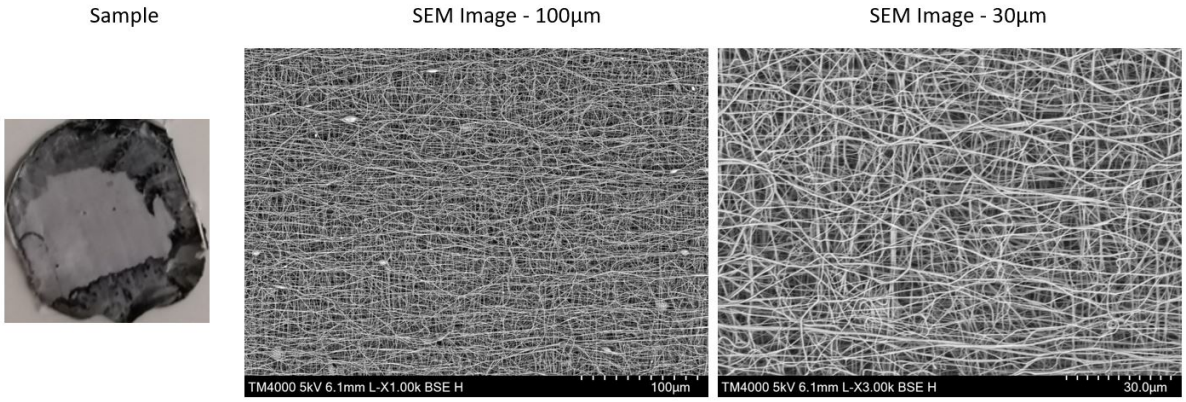

Figure 4.26: Sample 22 (trial nº16) and referent SEM image at two different scales.

Statistical Analysis

For each SEM image, three sets of measurements were assembled: fibre diameter, space between the fibres, and pore size. Figures 4.27 to 4.29 show three histograms that represent the averages of the space between the fibres, the fibre diameter, and the pore size for each experiment realized, as well as error bars representing the standard deviation for each test. Appendix A contains three tables with all the values used to create the histograms. It is essential to mention that, since the main goal is to measure the space between fibres, and the samples have ten layers of polymeric threads, only the last layer needs to, and should, be considered. This was achieved by altering the contrast and luminosity of the images to understand which fibres were the brightest, and thus, the ones belonging to the upper layer.

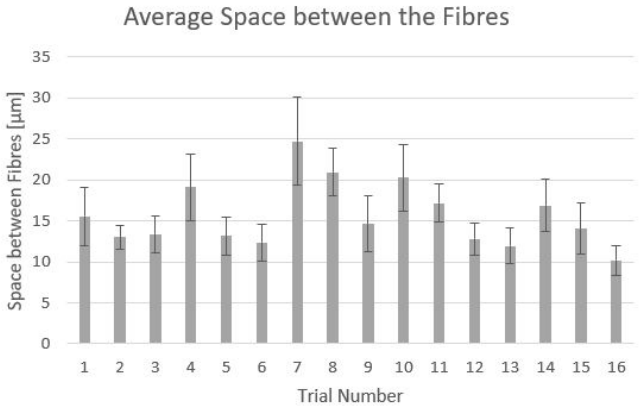

Figure 4.27: Histogram representing the average of space between fibres measured for each experimental trial.

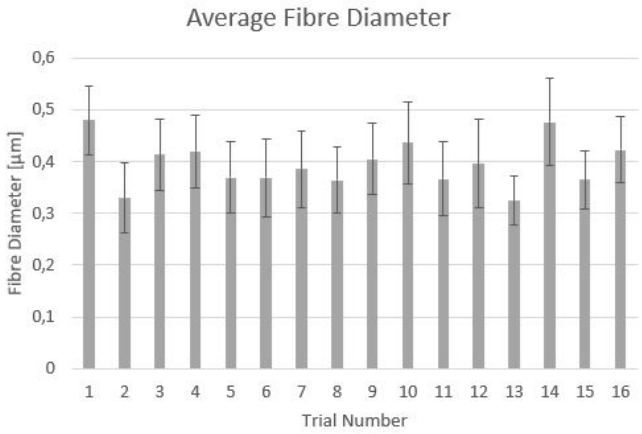

Figure 4.28: Histogram representing the average of fibre diameter measured for each experimental trial.

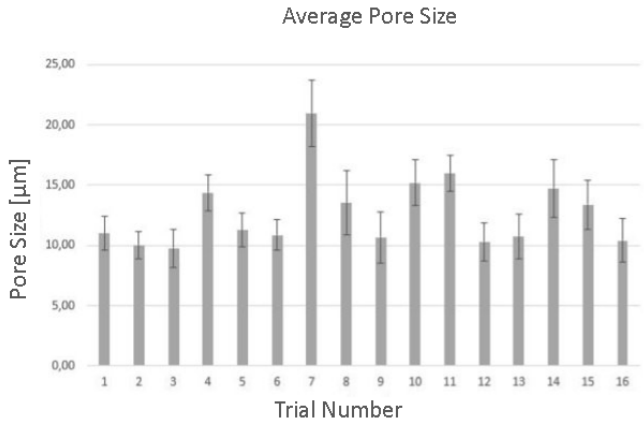

Figure 4.29: Histogram representing the average of pore sizes measured for each experimental trial.

Space between the Fibres

Using ImageJ, and after defining the right scale for the image, ten measurements of the distance between the most parallelly aligned fibres were made. Table A.1 contains the values for each sample taken into consideration in the DoE, as well as the average fibre spacing and the standard deviation. With the ten measurements made for each experimental trial, a statistical analysis was conducted using a three-factor ANOVA. Table 4.5 shows the calculations made by the software. Of all the information presented

in the ANOVA table, the primary interest will be focused on the value located in the "*p-value*" column, because this is the exact significance level of the factors. If the numbers found in this column are less than the critical value of alpha set by the experimenter - 0.05 -, then the effect is said to be significant.

Table 4.5: ANOVA table for the space between the fibres.

Factors & Interactions	*SS*	*df*	*MS*	*F*	*p-value*	*sig*
V_{bands}	415,906	5,000	83,181	3,429	0,007	yes
V_{table}	421,222	3,000	140,407	5,788	0,001	yes
F	*588,885*	*3,000*	196,295	*8,092*	*0,000*	yes
V_{bands} x V_{table}	283,062	15,000	18,871	0,778	0,699	no
V_{bands} x F	1099,347	15,000	73,290	3,021	0,001	yes
V_{table} x F	1125,434	9,000	125,048	5,155	0,000	yes

Therefore, analysing the table presented, it can be concluded that all the three independent factors have significance in the resulting space between the fibres on the deposition table. Moreover, the interactions between the flow rate (F) and the V_{bands}, as well as between the V_{table} and the flow rate (F), also show significance in the results. The next step is to understand precisely how, and how much, the factors, and the interaction between them, influence the results. In order to do that, and to have a better understanding of the ANOVA results, the measured values were processed to produce main effect plots and interaction plots.

The values presented in Figure 4.30 are the means at each level (high/low) under consideration for the parameters, stated in the DoE. Each graph has two points connected by a solid line. The steeper the gradient of the line, the more significant the difference between the two means and, consequently, the higher the influence of the factor. Thus, it can be concluded that the element that has the most impact on the space between the fibres is the velocity of the deposition table. When increasing the velocity of the deposition table from 125 to 750 [mm/min], the space between the fibres also increases, which was expected. The flow rate has a negative effect, as it can be seen by the slope of the line; when increasing the flow rate from 1.5 [mL/h] to 4 [mL/h], the space between the fibres will decrease, which was also expected. According to the theoretical assumptions discussed previously, the velocity od the collecting bands shouldn't affect at all the space between the fibres collected by the deposition table; however, as this

parameter value increases, the space between the resulting fibres also increases, as shown by the main effect plot graph. This states that the parameter has some effect on the results; however, since the slope of the line is not very high, the effect is not substantial.

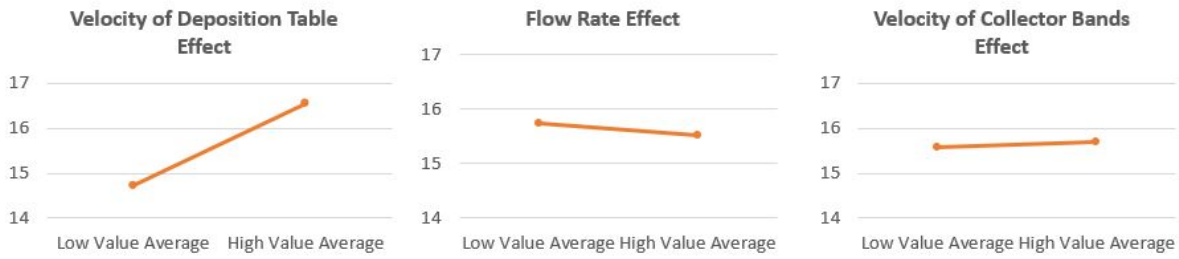

Figure 4.30: Effects of the input parameters in the space between fibres.

The interaction plots, shown in Figure 4.31, give indicators as to how the factors affect the output parameters in combination with each other. The indication is provided by the slope of the two lines of each plot, such as the less parallel the lines are, the more likely there is to be a significant interaction between the factors. Regarding the first interaction plot (velocity of bands and velocity of deposition table), since the line $V_{Table}(+)$ is, in general, higher than the $V_{Table}(-)$ it can be concluded that the main effect should be expected in this factor, such that high values of the table velocity lead to a higher space between the fibres. As for the main impact of the V_{Bands}, the average of the two points at the low levels needs to be estimated and compared with the average of the points at the high levels. Looking at the graph is hard to tell. Still, the average at higher levels of V_{Bands} is slightly bigger than at low levels; however, since it is not a significant difference, no main effect should be expected by the velocity of the collecting bands when interacting with the velocity of the deposition table. Even though there is an interaction between the two factors, as the graph proves, the ANOVA table states it is not a significant interaction for the results.

Regarding the interaction between the V_{Table} and flow rate, it is expected to exist, since the lines are not parallel at all. This type of interaction is usually called a cross-over interaction. The values of the line Flow Rate(-) are not higher or lower than the values of the line Flow Rate(+), so there is no main effect for flow rate when interacting with the velocity of the table. This is probably due to the fact that the velocity of the table shows a higher impact, in general, than the flow rate. Moreover, the average of values

at $V_{Table}(-)$ seems to be the same as the average at $V_{Table}(+)$. However, at $V_{Table}(+)$ the value is slightly higher, so the main effect of the velocity of the table is expected when interacting the flow rate, in such a way that the higher V_{Table}, the bigger the space between the fibres.

Finally, there is also an interaction between the V_{Bands} and the flow rate. For the same reasons mentioned for the previous graphs, there is no main effect of the flow rate, and, since the average of the two values at $V_{Bands}(+)$ is higher than at $V_{Bands}(-)$, it should be expected the main effect of the velocity of the bands when in conjugation with the flow rate. However, the impact is not very significant since the difference between the averages is almost inexistent.

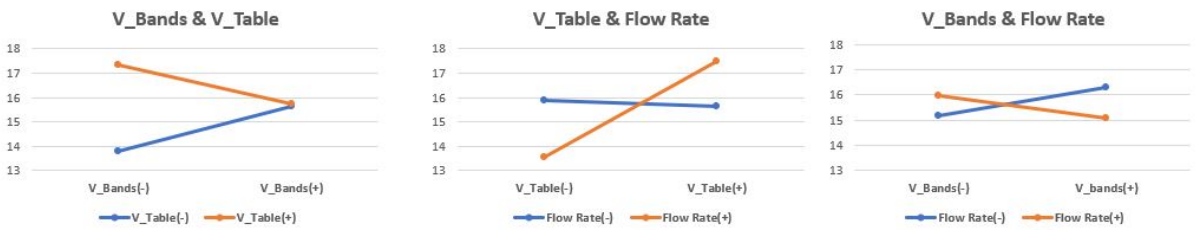

Figure 4.31: Interaction plots for space between fibres.

Fibre Diameter

The same analysis was conducted for the fibre diameter. Table A.2 contains the measurements made for each experimental trial, as well as the average, and the standard deviation of the fibre diameter. The three-factor ANOVA results for the data mentioned are presented in Table 4.6. As mentioned previously, the primary interest will be focused on the "*p-value*" column in order to understand which factors contain significance on the results (p-value <0.05). Thus, analysing the referent column, it can be seen that both the velocity of the collecting bands and the flow rate have some significance on the resulting diameter of the fibres. Moreover, both the interactions between the flow rate (F) and the velocity of the collecting bands (V_{Bands}), and the velocity of the deposition table (V_{Table}) and the velocity of the collecting bands, also have significance. These results were not expected.

Table 4.6: ANOVA table for the fibre diameter.

	SS	*df*	*MS*	*F*	*p-value*	*sig*
V_{Bands}	0,0884	5,0000	0,0177	5,5745	0,0001	yes
V_{Table}	0,0179	3,0000	0,0060	1,8807	0,1380	no
F	0,0379	3,0000	0,0126	3,9833	0,0101	yes
V_{Bands} x V_{Table}	0,1347	15,0000	0,0090	2,8306	0,0011	yes
V_{Bands} x F	0,1313	15,0000	0,0088	2,7587	0,0014	yes
V_{Table} x F	0,0252	9,0000	0,0028	0,8837	0,5427	no

The results of the fibre diameter measurements were also treated in order to create the main effect and interaction plots. As it can be seen in Figure 4.32, the parameter that has a more significant influence in the fibre diameter is the flow rate, as it is the line with the highest slope. The velocity of the collector bands also shows a significant effect on the fibre diameter, increasing the value of the width as the velocity of the bands increases. The parameter indicating the least amount of influence, and according to ANOVA, not presenting any significance, is the velocity of the deposition table.

Figure 4.32: Main effect plots for fibre diameter.

Analysing the interaction plots in Figure 4.33, it can be deduced that the flow rate interacts energetically with the velocity of the collecting bands; however, the main effect, when the two parameters interact, is expected to be the V_{Bands} since the average of the values at $V_{Bands}(+)$ is higher than at $V_{Bands}(-)$.

The lines in the plot of flow rate and V_{Table} do not cross each other, which leads to the belief that if there is an interaction between the two factors, it is very tiny. However, the line Flow Rate(-) is, in general, placed higher than the line Flow Rate(+), this means that the main effect should be expected in this factor, such that lower levels of flow flux lead to smaller diameters. The ANOVA table shows there is no significance in the

interaction between these two factors, which was expected since, by the time the fibres arrive at the deposition table, the diameter is already defined.

In the third plot, the lines come very close to crossing each other, which leads to believe there should be an interaction between the two factors and the main effect of the velocity of the bands should be expected given that the average of the points at $V_{Bands}(+)$ is substantially higher than at $V_{Bands}(-)$.

In theory, and based on previous studies on parameters influencing the fibre diameter in electrospinning, the flow rate should be the only factor with significance, since when the fibre reaches the collecting bands, and posteriorly, the deposition table, its diameter is already defined. However, these experimental results show a level of significance on the velocity of the collecting bands and on the interaction between the latter and the velocity of the deposition table, which makes it really hard to consider the experimental results on the fibre diameter as accurate.

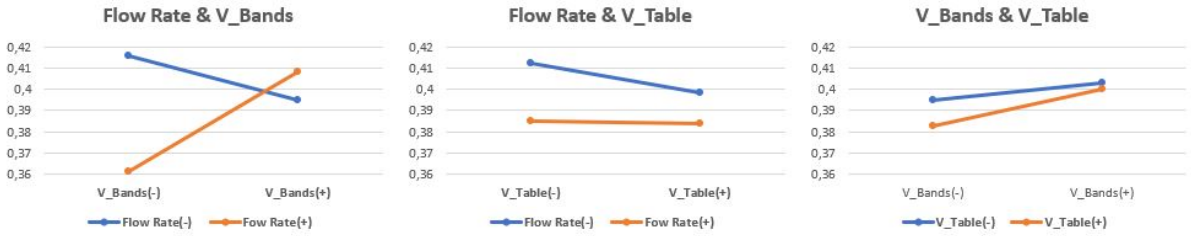

Figure 4.33: Interaction plots for fibre diameter.

Size of the Pores

Once again, the values present in Table A.3 are referent to the measurements of the pore size made for each experimental trial. The table also contains the average pore size for each experiment, as well as the standard deviation. It is important to mention that the measurements taken of the pore sizes were made considering the smallest distance (horizontally or vertically) of a pore. The three-factor ANOVA results for the data regarding the pore size are indicated in Table 4.7. Similarly to the previous analysis on the fibre diameter and the space between the fibres, the focus will be on the "*p-value*" column to understand which factors are significant to the results (p-value <0.05). Thus, it can be concluded, by analysing the table, that, similarly to the results from the space

between the fibres, all the three factors have significance on the results, as well as the interactions between the flow rate and the V_{Bands}, and the flow rate and the V_{Table}. It was expected that the same factors showed significance since the pore size is highly dependent on the space between the fibres.

Table 4.7: ANOVA table for the pore size.

	SS	*df*	*MS*	*F*	*p-value*	*sig*
V_{Bands}	34,0510	5,0000	6,8102	4,7783	0,0006	yes
V_{Table}	17,1581	3,0000	5,7194	4,0129	0,0097	yes
F	29,1496	3,0000	9,7165	6,8175	0,0003	yes
V_{Bands} x Vtable	6,0475	15,0000	0,4032	0,2829	0,9960	no
V_{Bands} x F	56,8373	15,0000	3,7892	2,6586	0,0021	yes
V_{Table} x F	32,5881	9,0000	3,6209	2,5406	0,0116	yes

Similarly to the previous analysis, the data retrieved was treated in order to create the main effect and interaction plots. As it can be seen in Figure 4.34, the parameter that has a more significant influence in the pore size is the velocity of the deposition table, which is in accord with the results from the effect analysis of the space between the fibres. The velocity of the bands shows a similar effect on the pore size to the one showed on the space between the fibres, such that higher values lead to bigger pore sizes, and, contrary to the conceptual model, and to the effect on the space between the fibres, the flow rate shows a positive impact. It should be expected the parameters behaved similarly to the space between the fibres, however, that is not the case for the flow rate. The fact that the measurements of the pore size took in consideration the smallest distance of the pore is probably the reason behind the difference on the calculation of the effect of the flow rate. The velocity of the deposition table, however, presents the higher effect on the pore sizes of the resulting fibre matrices, as it should be expected.

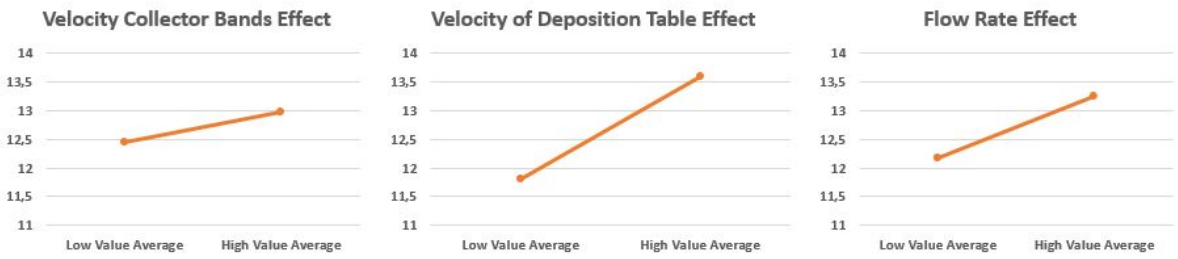

Figure 4.34: Main effect plots for pore size.

Analysing the interaction plots, in Figure 4.35, it can be verified that there is, in fact, an interaction between every pair of factors considered, even though not highly significant. For V_{Bands} and V_{Table} it can be concluded that the two elements have some interaction with each other, and the main effect should be expected by the velocity of the deposition table, such that higher values lead to more elevated pore sizes of the fibres.

As for the V_{Table} and flow rate, the two lines of flow rate levels cross each other right at the beginning, even though it's almost unnoticeable. This means that no main effect should be expected by the flow rate when in conjugation with the V_{Table}. Since the average between the values at $V_{Table}(+)$ is higher than at $V_{Table}(-)$ the main effect of the deposition table over the flow rate should be expected, such that higher values of the velocity of the table leads to more elevated pore sizes.

Regarding V_{Bands} and flow rate, the same can be concluded, since the average at $V_{Bands}(-)$ is higher than at $V_{Bands}(+)$, even though the difference is not notorious, the velocity of bands at low levels shows the main effect over the flow rate, when the two factors interact.

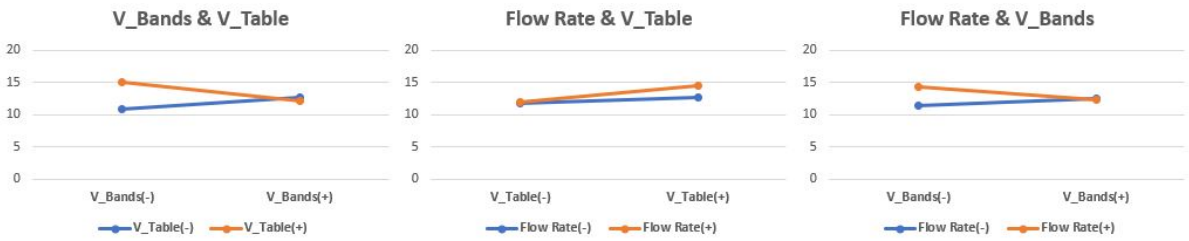

Figure 4.35: Interaction plots for pore size.

A number of reasons could be behind the changes in the results regarding the flow rate effect; however, the main one is the external factors which cannot be 100% controlled, nor accounted for. Electrospinning is a highly complex process, and in order to get results more accurate, it should have been conducted more experiments for a better statistical analysis.

ANOVA Regression Model for the Space between the Fibres

A linear equation was obtained with the coefficients calculated with ANOVA, which predicts the space between the fibres after the electrospinning process, having as base the experimental results. In general, the linear regression equation shows sufficiently good results in the prediction of the space between the fibres, with a standard error for the regression of 4,746, which means the experimental values tend to differ from the ones predicted by the ANOVA model on about 4%. The coefficients for each factor and interaction between factors, calculated by the ANOVA linear regression software are presented in Table 4.8, and the resulting equation is Equation 4.5. The comparison of the experimental results with the prediction of the ANOVA model is shown in Figure 4.36, where the similarity of the lines of the model with the experimental results is noticeable.

Table 4.8: Coefficients calculated by an ANOVA Regression.

	Coefficients
Constant (K)	15,687781
V_{Bands}	0,119644
V_{Table}	1,285094
F	0,108444
V_{Bands} x V_{Table}	-0,959369
V_{Bands} x F	-0,753919
V_{Table} x F	1,271981
V_{Bands} x V_{Table} x F	-0,662656

$$\begin{aligned} Space_{fibres} = {} & 0,1196 \cdot V_{Bands} + 1,285 \cdot V_{Table} + 0,108 \cdot F \\ & - 0,959 \cdot (V_{Bands} \cdot V_{Table}) - 0,754 \cdot (V_{Bands} \cdot F) \\ & + 1,272 \cdot (V_{Table} \cdot F) - 0,663 \cdot (V_{Bands} \cdot V_{Table} \cdot F) + K \qquad [\mu m] \end{aligned} \quad (4.5)$$

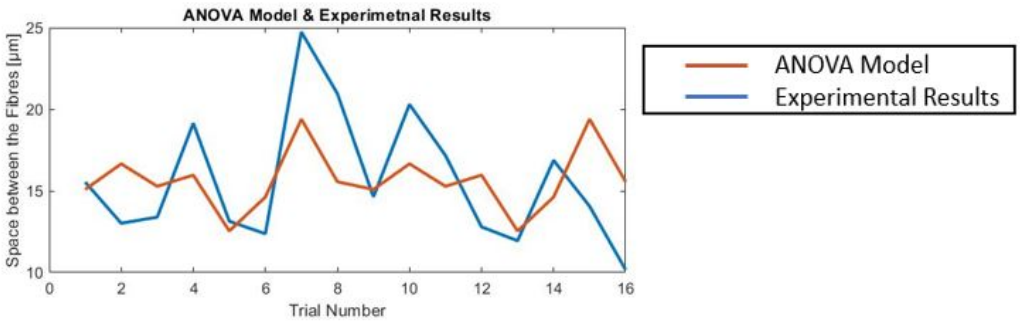

Figure 4.36: Plot comparing the experimental results with the ANOVA model predictions.

Comparison of Matlab results with Experimental results

As shown previously, a Matlab theoretical simulation was conducted in order to predict how the factors should influence the space between the fibres. Figure 4.37 shows the comparison of the conceptual model with the experimental results. The variance on the results is noticeable, which was somewhat expected. While the results from the experiments vary from 10 to 25 µm, the theoretical model range of values goes from 10 to 120 µm. The difference in ranges is notorious, and it comes from the fact that, in theory, several external factors cannot be accounted for. Moreover, the theoretical model assumes the three parameters have the same percentage of relevance on the results, and, as seen previously on the statistical analysis, that is not the case.

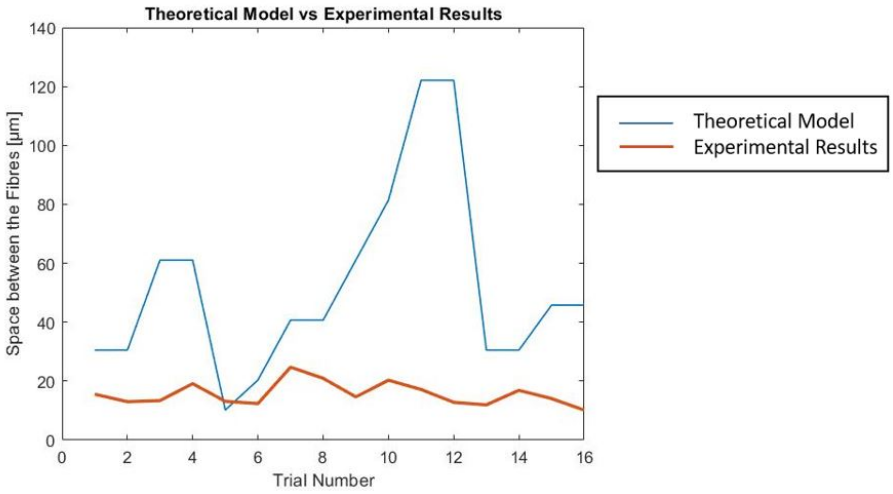

Figure 4.37: Theoretical model comparison with experimental results.

The model can, however, predict how the variations on the input parameters will affect the space between the fibres - increase it or decrease it. The theoretical model can also be optimized by adding some adjustment constants that consider the level of significance of each factor. Figure 4.38 shows the result when the theoretical equation is adapted by taking the effect of parameters into consideration. A significant change can be seen on the outcome results; the range of values is now closer to the scope of the experimental trials - from 5 to 35 µm. However, it is still not an accurate prediction since there is a substantial variance between the experimental results and the model's prediction, having an overall average of error of 30%, which is a highly significant value for an error percentage.

This outcome is to be expected since electrospinning is a highly complex process, and there are always external factors affecting the results that, in theory, cannot be accounted for.

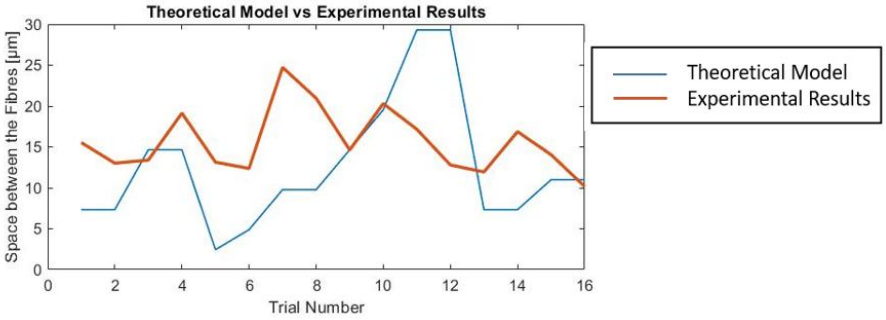

Figure 4.38: Optimized theoretical model comparison with experimental results.

4.5.3 Discussion

A significant part of the results obtained was in accord with the expectations from an overall analysis of the equipment components and how its response should be when submitted to different input values. There were, however, a few results that were not expected and did not seem to be an accurate representation of the reality of the process. For instance, regarding the fibre diameter, the ANOVA statistical analysis showed that the velocity of the collecting bands have significance on the resulting fibre diameter and, it is known, that such a conclusion is not accurate since, by the time the fibre is collected by the bands, its width is already defined due to the flow rate and the distance

existing between the spinneret's tip and the collector bands. The inaccurate result is probably due to errors in the measurements of the fibre diameter, using the software ImageJ. There is a chance that, while assuming to be measuring the diameter of only one fibre, it was actually being estimated the diameter of a collection of threads that were overlapped.

Both the space between the fibres and the pore size results were in accord with the expectations. All the parameters should behave similarly in the analysis of these two variables since the size of the pores is highly related to the space between the fibres. There was, however, a difference in the behaviour of the flow rate in the two variables. While on the space between the fibres, the flow rate has a negative effect - decreasing the space between the fibres as its value increases -, when it comes to the pore size, the flow rate showed a positive impact - increasing the pore size as its value increases. The outcome that was expected based on the theoretical analysis was the first one. As mentioned previously, the measurements of the pore size took into consideration the smallest distance of the pore; this is not significantly different from the measures retrieved from the space between the fibres; however, it could be the reason behind the unusual behaviour of the flow rate when it comes to the pore size. Moreover, the velocity of the collecting bands also showed significance in both the space between the fibres and pore size; this was not expected since it was assumed by the theoretical model that this parameter shouldn't affect the disposal of the fibre on the deposition table, even though, it should affect it on the collecting bands.

Regarding the MATLAB theoretical simulation, as mentioned previously, the predictions cannot be 100% trusted. Being a purely theoretical model, with no influence of concepts retrieved from a practical point of view, it is challenging to obtain a high level of accuracy on the results. Not being fully satisfied with the results from the model, optimization was performed, making use of the statistical analysis results; however, the error percentage was still extremely high. In contrast to this model, the ANOVA model, resulting from a linear regression analysis, was obtained purely based on experimental results and had a percentage of error below the 5%, which shows the model is capable of excellent predictions of the space between the fibres.

Intentionally blank page.

Chapter 5

Conclusions and Future Work

Electrospinning is a simple, unique, versatile, and cost-effective technique that is widely used for the fabrication of aligned nanofibres. The morphology of the nanofibres is significantly affected by the various parameters such as polymer concentration, viscosity, molecular weight, applied voltage, tip-to-collector distance and solvent. However, in the context of this dissertation, different parameters were analysed in order to understand if, and how, they would affect specific characteristics of the resulting nanofibres. Since the electrospinning equipment used had incorporated in it both moving collecting and deposition modules, the input parameters were the velocity of the collector bands, the velocity of the deposition table and the flow rate, as mentioned through the dissertation. Chapter 4 explains the procedure through the entire performance of the experimental trials, and analyses and discusses its results. In summary, the three factors show significance for the space between the fibres and the pore size. It is notorious that, for these two output variables, the parameter with higher effect on the results is the velocity of the deposition table, such that higher values of this parameter lead to bigger space between the fibres and bigger pore sizes. The velocity of the collecting bands also showed similar effects on both the space between te fibres and the pore size, such that higher values for this parameter lead to higher space between the fibres and bigger pore sizes. The flow rate showed a negative effect on the space between the fibres, such that increasing its value leads to smaller distance between the fibres. However, it shows an opposite behaviour on the pore size, having a positive effect. The reason behind these results probably lays on the fact that, during the measurements of the output variables, errors could have occurred. As mentioned at the beginning of the description of the experimen-

tal part, the experiments done with the electrospinning equipment were conducted with five repetition cycles for each orientation of the deposition table (0°and 90°), this means that, in total, the experimental samples had ten layers of fibres. When measuring the different output parameters, it was essential to choose the fibres belonging to the same layer carefully; however, the number of existing layers did not make it an easy task, and there is a chance some of the measurements performed were in fact "fake values", which could be on the origin of the variance of the flow rate effect on the pore sizes. In order to prevent possible errors on data retrieving from the experiment results in further studies on how these parameters affect the process, only samples with one layer of fibres should be taken into consideration for the analysis. Furthermore, electrospinning is a very complex process, and there is a chance that external factors, which cannot be accounted for, could have affected the results. In order to eliminate the randomness of the process, and consequently, the effect of the uncontrollable external factors, more experiments should have been conducted and accounted for in the statistical analysis.

The resulting model of the ANOVA statistical analysis showed, that, for the space between the fibres, all the three factors have statistical significance, even though, it is noticeable that the velocity of the deposition table contains a much higher effect over the velocity of the collecting bands and the flow rate. The model resulting from a statistical linear regression, which predicts the result of the space between the fibres, presented excellent results. However, an optimisation to it should also be conducted in order to reduce even more the percentual error. This can be achieved by performing more experiments and inserting the resulting data into the ANOVA calculations. The same can be stated for the theoretical model developed. The model should take into consideration how much each parameter affects the results and, maybe, even consider the interaction existent between factors. This can be performed making use of the statistical analysis performed throughout this dissertation.

The study on how the various parameters of the electrospinning process affect its results is of great importance, since electrospun nanofibres have found numerous potential applications in almost every field, including enzyme immobilisation, sensing membranes, protective clothing, wound healing and of, course, bone and cartilage tissue engineering. The study on how to control the alignment of the nanofibres is essential since one of

the limitations of the resulting electrospun nanofibre scaffolds is that cells show reduced infiltration into it. Controlling the arrangement, and thus the space between the fibres is one step closer to the making of 3D scaffolds with the perfect pore sizes for cell infiltration. Moreover, the results showed that the parameter with a more significant impact on the space between the fibres is the velocity of the deposition table. Thus, inserting a moving deposition module, with both linear and rotational movement, to electrospinning equipments is of great help to control the fibre alignment, allowing significant progress for the construction of tissue-engineered cartilage, since it facilitates the replication of the native tissue's complex fibrillar organisation. Thus, allowing to create engineered tissues with anisotropic mechanical properties, similar to the native tissue of cartilage.

Intentionally blank page.

Bibliography

[1] M. Kotecha, Z. Yin, and R. L. Magin, "Magnetic Resonance in the Assessment of Tissue Engineered Cartilage," in *Biophysics and Biochemistry of Cartilage by NMR and MRI*, 2016, ch. 20.

[2] A. J. Sophia Fox, A. Bedi, and S. A. Rodeo, "The basic science of articular cartilage: Structure, composition, and function," *Sports Health*, vol. 1, no. 6, pp. 461–468, 2009.

[3] A. Completo and F. Fonseca, *Fundamentos de Biomecânica Músculo, Esquelética e Ortopédica*. Publindústria, 2011.

[4] C. Patrícia and C. Fernandes, "Otimização do processo de fabricação e semeação de scaffolds de PCL/Gelatina anisotrópicos para a engenharia de cartilagem," Ph.D. dissertation, University of Aveiro, 2018.

[5] K. Pal and I. Banerjee, "Polymeric gels for cartilage tissue engineering," in *Polymeric Gels: Characterization, Properties and Biomedical Applications*, 2018, ch. 20.

[6] "Cartilage," 2019. [Online]. Available: https://biologydictionary.net/cartilage/

[7] "Boundless Anatomy and Physiology: Cartilage." [Online]. Available: https://courses.lumenlearning.com/boundless-ap/chapter/cartilage/

[8] "Cartilage Anatomy," 2018. [Online]. Available: https://www.britannica.com/science/cartilage

[9] S. Bryce, "What is Cartilage? - Definition, Types & Function." [Online]. Available: https://study.com/academy/lesson/what-is-cartilage-function-definition-types.html

[10] B. L. Wong, "Biomechanics of Cartilage Articulation: Effects of degeneration, lubrification, and focal articular defects," Ph.D. dissertation, University of California, 2009.

[11] G. Bellucci and B. B. Seedhom, "Mechanical behaviour of articular cartilage under tensile cyclic load," pp. 1337–1345, 2001.

[12] J. M. Mansour, "Biomechanics of cartilage," in *Kinesiology: The Mechanics and Pathomechanics of Human Movement*, 2nd ed. Lippincott Williams AND Wilkins, 2013, ch. 5, pp. 69–83.

[13] "Synovial Joints." [Online]. Available: https://www.jobilize.com/anatomy/course/9-4-synovial-joints-joints-by-openstax?page=103{&}=

[14] S. J. Abbass and F. M. Abdulateef, "Finite Element Analysis of Human and Artificial Articular Cartilage," *Journal of Engineering*, vol. 18, no. 4, pp. 443–458, 2012.

[15] F. Boschetti, G. Pennati, and F. Gervaso, "Biomechanical properties of human articular cartilage under compressive loads," no. June 2014, 2004.

[16] V. C. Mow and X. E. Guo, "Mechano-Electrochemical Properties Of Articular Cartilage: Their Inhomogeneities and Anisotropies," *Annual Review of Biomedical Engineering*, vol. 4, no. 1, pp. 175–209, 2002.

[17] R. B. Martin, D. B. Burr, and N. A. Sharkey, *Synovial Joint Mechanics. In: Skeletal Tissue Mechanics.* Springer, New York, NY. [Online]. Available: https://musculoskeletalkey.com/synovial-joint-mechanics/

[18] D. R. Carter and M. Wong, "Modelling cartilage mechanobiology," *Philosophical Transactions of the Royal Society B: Biological Sciences*, vol. 358, no. 1437, pp. 1461–1471, 2003.

[19] R. F. Ker, "The design of soft collagenous load-bearing tissues," *Journal of Experimental Biology*, vol. 202, no. 23, pp. 3315–3324, 1999.

[20] Y. Sasazaki, R. Shore, and B. B. Seedhom, "Deformation and failure of cartilage in the tensile mode," *Journal of Anatomy*, vol. 208, no. 6, pp. 681–694, 2006.

[21] C. Y. Huang, V. C. Mow, and G. A. Ateshian, "The role of flow-independent viscoelasticity in the biphasic tensile and compressive responses of articular cartilage," *Journal of Biomechanical Engineering*, vol. 123, no. 5, pp. 410–417, 2001.

[22] V. Roth and V. C. Mow, "The intrinsic tensile behavior of the matrix of bovine articular cartilage and its variation with age." *J Bone Joint Surg*, 1980.

[23] M. B. Schimdt, V. C. Mow, L. E. Chun, and D. R. Eyre, "Effects of proteoglycan extraction on the tensile behavior of articular cartilage." *J Orthop Res.*, 1990.

[24] W. Zhu, V. C. Mow, T. J. Koob, and D. R. Eyre, "Viscoelastic shear properties of articular cartilage and the effects of glycosidase treatments," *Journal of Orthopaedic Research*, vol. 11, no. 6, pp. 771–781, 1993.

[25] W. Ross, "Cartilage Mechanics," 2017. [Online]. Available: https://slideplayer.com/slide/10947797/

[26] V. C. Mow, W. Gu, and F. H. Chen, "Structure and function of articular cartilage and meniscus," 2005.

[27] G. E. Kempson, H. Muir, S. A. Swanson, and M. A. Freeman, "Correlations between stiffness and the chemical constituents of cartilage on the human femoral head," *BBA - General Subjects*, vol. 215, no. 1, pp. 70–77, 1970.

[28] C. Armstrong and V. C. Mow, "Variations in the intrinsic mechanical properties of human articular cartilage with age, degeneration, and water content." *Journal of Bone and Joint Surgery-American Volume*, 1982.

[29] J. Lane, E. Chisena, and J. Black, "Experimental knee instability: early mechanical property changes in articular cartilage in a rabbit model." *Clin Orthop Relat Res*, 1979.

[30] Â. Semitela, A. F. Girão, C. Fernandes, P. A. A. P. Marques, and A. Completo, "Desenvolvimento de scaffolds anisotrópicos de PCL e gelatina para a regeneração de cartilagem," p. 106827, 2014.

[31] B. P. Chan and K. W. Leong, "Scaffolding in tissue engineering: General approaches and tissue-specific considerations," *European Spine Journal*, vol. 17, no. SUPPL. 4, 2008.

[32] M. Gren, "Living cell products as wound healing biomaterials: Current and future modalities," in *Wound Healing Biomaterials: Volume 1: Therapies and Regeneration*. Woodhead Publishing, 2016.

[33] T. Garg, O. Singh, S. Arora, and R. S. Murthy, "Scaffold: A novel carrier for cell and drug delivery," *Critical Reviews in Therapeutic Drug Carrier Systems*, vol. 29, no. 1, pp. 1–63, 2012.

[34] Z. Izadifar, X. Chen, and W. Kulyk, "Strategic Design and Fabrication of Engineered Scaffolds for Articular Cartilage Repair," *Journal of Functional Biomaterials*, vol. 3, no. 4, pp. 799–838, 2012.

[35] P. R. Fernandes and P. Bártolo, *Tissue Engineering: Computer Modeling, Biofabrication and Cell Behavior*. Springer Netherlands, 2014.

[36] Y. Morsi, C. Wong, and S. Patel, "Virtual Prototyping of Biomanufacturing in Medical Applications," in *Virtual Prototyping & Bio Manufacturing in Medical Applications*, 2008.

[37] Y. Ikada, *Tissue Engineering: Fundamentals and Applications*. Academic Press, 2006.

[38] N. Zhu and X. Chen, "Biofabrication of Tissue Scaffolds," in *Advances in Biomaterials Science and Biomedical Applications*, 2013, ch. 12.

[39] L. Papadimitriou, P. Manganas, A. Ranella, and E. Stratakis, "Biofabrication for neural tissue engineering applications," *Materials Today Bio*, vol. 6, no. December 2019, p. 100043, 2020. [Online]. Available: https://doi.org/10.1016/j.mtbio.2020.100043

[40] M. Abu Ghalia and Y. Dahman, "Advanced nanobiomaterials in tissue engineering," in *Nanobiomaterials in Soft Tissue Engineering*. William Andrew, 2016, ch. 6.

[41] T. Woodfield, K. Lim, P. Morouço, R. Levato, J. Malda, and F. Melchels, "Biofabrication in tissue engineering," in *Reference Module in Materials Science and Materials Engineering*. Elsevier Inc., 2017, no. September, ch. 5, pp. 236–266.

[42] G. Cidonio, M. Glinka, J. Dawson, and R. Oerffo, "The cell in the ink: Improving biofabrication by printing stem cells for skeletal regenerative medicine," *Biomaterials*, 2019.

[43] K. Dzobo, N. E. Thomford, D. A. Senthebane, H. Shipanga, A. Rowe, C. Dandara, M. Pillay, and K. S. C. M. Motaung, "Advances in regenerative medicine and tissue engineering: Innovation and transformation of medicine," *Stem Cells International*, vol. 2018, 2018.

[44] P. Rider, Ž. P. Kačarević, S. Alkildani, S. Retnasingh, R. Schnettler, and M. Barbeck, *Additive manufacturing for guided bone regeneration: A perspective for alveolar ridge augmentation*, 2018, vol. 19, no. 11.

[45] G. Lee and J. Barlow, "Selective laser sintering of bioceramic materials for implants," *Proceedings of the solid freeform fabrication*, pp. 376–380, 1996.

[46] L. Hao, M. Savalani, and R. Harris, "Layer manufacturing of polymer/bioceramic implants for bone replacement and tissue growth." *International Conference on Advanced Research and Rapid Prototyping; Virtual modeling and rapid manufacturing*, 2005.

[47] R. J. Mondschein, A. Kanitkar, C. B. Williams, S. S. Verbridge, and T. E. Long, "Polymer structure-property requirements for stereolithographic 3D printing of soft tissue engineering scaffolds," *Biomaterials*, vol. 140, pp. 170–188, 2017.

[48] S. A. Skoog, P. L. Goering, and R. J. Narayan, "Stereolithography in tissue engineering," *Journal of Materials Science: Materials in Medicine*, vol. 25, no. 3, pp. 845–856, 2014.

[49] C. De Maria, "Fused Deposition Modelling," 2015. [Online]. Available: https://pt.slideshare.net/biofabrication{_}unipi/2015-1015-fused-deposition-modelling-56368529

[50] M. Adel, O. Abdelaal, A. Gad, A. B. Nasr, and A. M. Khalil, "Polishing of fused deposition modeling products by hot air jet: Evaluation of surface roughness," *Journal of Materials Processing Technology*, vol. 251, pp. 73–82, 2018. [Online]. Available: http://dx.doi.org/10.1016/j.jmatprotec.2017.07.019

[51] W. Jefford, C, T. Kabengele, J. Kovacs, and U. Burger, "Eletrofiação: Uma alternativa para a produção de não tecidos." *Revista da UNIFEBE*, vol. 3, no. 1, pp. 257–260, 1974.

[52] D. Li, Y. Wang, and Y. Xia, "Electrospinning of polymeric and ceramic nanofibers as uniaxially aligned arrays," *Nano Letters*, vol. 3, no. 8, pp. 1167–1171, 2003.

[53] C. M. Hsu and S. Shivkumar, "Nano-sized beads and porous fiber constructs of Poly(ϵ-caprolactone) produced by electrospinning," *Journal of Materials Science*, vol. 39, no. 9, pp. 3003–3013, 2004.

[54] D. Li and Y. Xia, "Direct fabrication of composite and ceramic hollow nanofibers by electrospinning," *Nano Letters*, vol. 4, no. 5, pp. 933–938, 2004.

[55] M. Afshari, *Electrospun nanofibers*, 2016.

[56] J. Xue, T. Wu, Y. Dai, and Y. Xia, "Electrospinning and Electrospun Nanofibers: Methods, Materials, and Applications," *Physiology & behavior*, vol. 176, no. 3, pp. 139–148, 2019.

[57] D. Parajuli, P. Koomsap, A. A. Parkhi, and P. Supaphol, "Experimental investigation on process parameters of near-field deposition of electrospinning-based rapid prototyping," *Virtual and Physical Prototyping*, vol. 11, no. 3, pp. 193–207, 2016.

[58] Y.-K. Fuh, "Fabrication of monolithic polymer nanofluidic channels via near-field electrospun nanofibers as sacrificial templates," *Journal of Micro/Nanolithography, MEMS, and MOEMS*, vol. 10, no. 4, p. 043004, 2011.

[59] D. Shin, J. Kim, and J. Chang, "Experimental study on jet impact speed in near-field electrospinning for precise patterning of nanofiber," *Journal of Manufacturing Processes*, vol. 36, no. June, pp. 231–237, 2018.

[60] C. H. Park, H. R. Pant, and C. S. Kim, "Novel robot-assisted angled multi-nozzle electrospinning set-up: Computer simulation with experimental observation of electric field and fiber morphology," *Textile Research Journal*, vol. 84, no. 10, pp. 1044–1058, 2014.

[61] S. A. Theron, A. L. Yarin, E. Zussman, and E. Kroll, "Multiple jets in electrospinning: Experiment and modeling," *Polymer*, vol. 46, no. 9, pp. 2889–2899, 2005.

[62] F. L. Zhou, R. H. Gong, and I. Porat, "Mass production of nanofibre assemblies: By electrostatic spinning," *Polymer International*, vol. 58, no. 4, pp. 331–342, 2009.

[63] H. S. SalehHudin, E. N. Mohamad, W. N. L. Mahadi, and A. Muhammad Afifi, "Multiple-jet electrospinning methods for nanofiber processing: A review," *Materials and Manufacturing Processes*, vol. 33, no. 5, pp. 479–498, 2018.

[64] N. M. Thoppey, J. R. Bochinski, L. I. Clarke, and R. E. Gorga, "Unconfined fluid electrospun into high quality nanofibers from a plate edge," *Polymer*, vol. 51, no. 21, pp. 4928–4936, 2010.

[65] H. J. Yu, S. V. Fridrikh, and G. C. Rutledge, "Production of submicrometer diameter fibers by two-fluid electrospiiming," *Advanced Materials*, vol. 16, no. 17, pp. 1562–1566, 2004.

[66] "Coaxial Electrospinning." [Online]. Available: https://nanotechnologysolutions.wordpress.com/2013/07/29/coaxial-electrospinning/

[67] Z. Ding, A. Salim, and B. Ziaie, "Selective nanofiber deposition through field-enhanced electrospinning," *Langmuir*, vol. 25, no. 17, pp. 9648–9652, 2009.

[68] J. A. Matthews, G. E. Wnek, D. G. Simpson, and G. L. Bowlin, "Electrospinning of collagen nanofibers," *Biomacromolecules*, vol. 3, no. 2, pp. 232–238, 2002.

[69] V. Beachley, E. Katsanevakis, Z. Ning, and X. Wen, "Highly Aligned Polymer Nanofiber Structures: Fabrication and Applications in Tissue Engineering," in *Biomedical Applications of Polymeric Nanofibers*. Springer, New York, NY.

[70] E. Smit, U. Buttner, and R. D. Sanderson, "Continuous yarns from electrospun fibers," *Polymer*, vol. 46, no. 8, pp. 2419–2423, 2005.

[71] L. Meli, J. Miao, J. S. Dordick, and R. J. Linhardt, "Electrospinning from room temperature ionic liquids for biopolymer fiber formation," *Green Chemistry*, vol. 12, no. 11, pp. 1883–1892, 2010.

[72] W. E. Teo and S. Ramakrishna, "A review on electrospinning design and nanofibre assemblies," *Nanotechnology*, vol. 17, no. 14, 2006.

[73] P. Dalton, D. Klee, and M. Möller, "Electrospinning with dual collection rings," *Polymer*, vol. 46, pp. 611–614, 01 2005.

[74] Y. Ying, J. Zhidong, and G. Zhicheng, "Controlled deposition of electrospun poly (ethylene oxide) fibers via insulators," *2005 IEEE International Conference on Dielectric Liquids, ICDL 2005*, pp. 457–460, 2005.

[75] J. M. Deitzel, J. D. Kleinmeyer, J. K. Hirvonen, and N. C. Beck Tan, "Controlled deposition of electrospun poly(ethylene oxide) fibers," *Polymer*, vol. 42, no. 19, pp. 8163–8170, 2001.

[76] S. H. Huang, T. C. Chien, K. Y. Hung, and Y. C. Chung, "Selective deposition of electrospun alginate-based nano-fibers on cell-repelling hydrogel surfaces for cell-based microarray," *14th International Conference on Miniaturized Systems for Chemistry and Life Sciences 2010, MicroTAS 2010*, vol. 3, no. March, pp. 1892–1894, 2010.

[77] L. Buttafoco, N. G. Kolkman, P. Engbers-Buijtenhuijs, A. A. Poot, P. J. Dijkstra, I. Vermes, and J. Feijen, "Electrospinning of collagen and elastin for tissue engineering applications," *Biomaterials*, vol. 27, no. 5, pp. 724–734, 2006.

[78] D. Yang, B. Lu, Y. Zhao, and X. Jiang, "Fabrication of aligned fibrous arrays by magnetic electrospinning," *Advanced Materials*, vol. 19, no. 21, pp. 3702–3706, 2007.

[79] Y. Liu, X. Zhang, Y. Xia, and H. Yang, "Magnetic-field-assisted electrospinning of aligned straight and wavy polymeric nanofibers," *Advanced Materials*, vol. 22, no. 22, pp. 2454–2457, 2010.

[80] K. Dhirendra S., N. Amit, and S. R. Mohan, "Electrospinning Apparatus For Producing Nanofibers and Process Thereof," 2009. [Online].

Available: https://worldwide.espacenet.com/patent/search/family/040522584/publication/US2009091065A1?q=Electrospinningapparatusalignedfiber

[81] C. Hongbo, D. Yumei, L. Haoyi, W. Weifeng, and Y. Weimin, "Electrostatic spinning orientation fiber preparation device," 2014. [Online]. Available: https://worldwide.espacenet.com/patent/search/family/051850502/publication/CN104141174A?q=electrospinningfiberorientedapparatus

[82] Y. Mohammadi, "Apparatus and method for electrospinning 2D- or 3D-structures of micro- or nano-fibrous materials," 2007. [Online]. Available: https://worldwide.espacenet.com/patent/search/family/039111600/publication/EP2045375A1?q=Electrospinningapparatusalignedfiber3D

[83] O. Iordache, "Design of Experiments and Analysis," *Polytope Projects*, pp. 181–190, 2013.

[84] R. Fisher, *The Design of Experiments*, 1935.

[85] N. K. Sahu and A. Andhare, "Design of Experiments Applied to Industrial Process," in *Statistical Approaches With Emphasis on Design of Experiments Applied to Chemical Processes*, 2018, ch. 2.

[86] K. Nasouri and A. Haji, "A Novel Study of Electrospun Nanofibers Morphology as a Function of Polymer Solution Properties," no. September, pp. 1–5, 2013.

[87] M. da Silva Bastos, "Projeto de um sistema automatizado de fabricação de enxertos de cartilagem em grande-escala," Ph.D. dissertation, Universidade de Aveiro, 2019.

[88] P. Stafiej, F. Küng, D. Thieme, M. Czugala, F. E. Kruse, D. W. Schubert, and T. A. Fuchsluger, "Adhesion and metabolic activity of human corneal cells on PCL based nanofiber matrices," *Materials Science and Engineering C*, vol. 71, pp. 764–770, 2017. [Online]. Available: http://dx.doi.org/10.1016/j.msec.2016.10.058

[89] N. S. Binulal, A. Natarajan, D. Menon, V. K. Bhaskaran, U. Mony, and S. V. Nair, "PCL-gelatin composite nanofibers electrospun using diluted acetic acid-ethyl acetate solvent system for stem cell-based bone tissue engineering," *Journal of Biomaterials Science, Polymer Edition*, vol. 25, no. 4, pp. 325–340, 2014.

[90] K. Ren, Y. Wang, T. Sun, W. Yue, and H. Zhang, "Electrospun PCL/gelatin composite nanofiber structures for effective guided bone regeneration membranes," *Materials Science and Engineering C*, vol. 78, pp. 324–332, 2017. [Online]. Available: http://dx.doi.org/10.1016/j.msec.2017.04.084

Appendix A

Results

Table A.1: Measurements of the spacing between the fibres, in μm.

Sample	Trial nº	Measure 1	Measure 2	Measure 3	Measure 4	Measure 5	Measure 6	Measure 7	Measure 8	Measure 9	Measure 10	Average	Standard Deviation
15	1	13,99	12,31	25,49	13,21	15,43	13,60	13,50	17,65	13,33	16,88	15,54	3,52
10	2	14,51	15,23	13,86	11,47	15,43	12,13	11,48	11,21	13,06	11,76	13,01	1,48
2	3	15,11	12,13	16,09	12,40	10,41	17,46	13,85	11,91	9,84	14,72	13,39	2,24
11	4	22,30	20,34	22,02	20,93	11,93	12,34	23,28	14,48	19,97	23,78	19,14	4,07
7	5	13,92	9,51	12,88	10,80	11,47	12,50	17,74	14,71	11,82	16,02	13,13	2,26
16	6	12,55	12,29	14,90	15,17	12,29	11,25	15,96	7,45	10,99	10,85	12,37	2,27
14	7	34,79	20,33	34,57	26,77	20,20	23,00	22,33	22,60	17,28	25,42	24,73	5,32
5	8	23,45	25,22	23,85	18,94	19,51	16,55	23,27	22,66	20,50	15,57	20,95	2,95
3	9	13,36	14,88	12,05	12,58	14,46	12,02	11,87	12,22	19,88	23,00	14,63	3,44
23	10	16,48	21,85	27,79	23,26	23,64	17,88	24,22	13,37	16,28	18,20	20,30	4,08
19	11	20,75	18,56	17,44	21,53	15,65	15,80	15,73	17,62	12,92	15,62	17,16	2,35
20	12	15,30	12,39	11,68	11,57	12,19	14,40	15,79	9,42	15,01	10,18	12,79	2,00
17	13	10,33	12,51	9,42	9,02	10,20	15,60	12,39	15,30	10,59	14,06	11,94	2,17
18	14	19,61	22,90	12,29	17,14	19,48	12,29	19,35	15,17	16,47	13,99	16,87	3,16
21	15	13,06	20,22	15,52	16,57	12,01	10,57	12,11	10,58	18,53	11,37	14,05	3,12
22	16	9,78	6,91	8,58	8,09	11,49	9,92	11,09	13,08	12,35	10,30	10,16	1,74

Table A.2: Fibre Diameter measurements, in μm.

Sample	Trial nº	Measure 1	Measure 2	Measure 3	Measure 4	Measure 5	Measure 6	Measure 7	Measure 8	Measure 9	Measure 10	Average	Standard Deviation
15	1	0,410	0,513	0,391	0,528	0,513	0,564	0,473	0,487	0,363	0,552	0,479	0,063
10	2	0,361	0,375	0,314	0,258	0,391	0,304	0,258	0,301	0,260	0,475	0,330	0,064
2	3	0,321	0,441	0,462	0,516	0,326	0,516	0,426	0,413	0,365	0,344	0,413	0,066
11	4	0,462	0,462	0,462	0,344	0,410	0,566	0,312	0,410	0,359	0,410	0,420	0,066
7	5	0,310	0,394	0,310	0,426	0,413	0,413	0,206	0,437	0,413	0,372	0,369	0,066
16	6	0,354	0,308	0,411	0,424	0,398	0,514	0,411	0,332	0,308	0,230	0,369	0,072
14	7	0,308	0,462	0,373	0,388	0,410	0,423	0,437	0,391	0,205	0,459	0,386	0,071
5	8	0,309	0,258	0,372	0,361	0,467	0,412	0,464	0,309	0,330	0,361	0,364	0,061
3	9	0,414	0,411	0,361	0,343	0,465	0,565	0,308	0,360	0,411	0,411	0,405	0,065
23	10	0,364	0,385	0,364	0,337	0,462	0,365	0,538	0,544	0,544	0,462	0,437	0,076
19	11	0,385	0,261	0,328	0,459	0,381	0,328	0,256	0,423	0,373	0,473	0,367	0,067
20	12	0,514	0,347	0,459	0,308	0,304	0,411	0,347	0,411	0,553	0,308	0,396	0,081
17	13	0,274	0,379	0,379	0,365	0,274	0,309	0,350	0,240	0,353	0,325	0,325	0,044
18	14	0,370	0,581	0,524	0,514	0,553	0,326	0,553	0,424	0,403	0,514	0,476	0,080
21	15	0,358	0,437	0,304	0,307	0,309	0,309	0,391	0,466	0,412	0,360	0,365	0,054
22	16	0,456	0,391	0,459	0,513	0,410	0,410	0,410	0,324	0,523	0,328	0,422	0,061

Table A.3: Measurements of the pore sizes, in μm.

Sample	Trial nº	Measure 1	Measure 2	Measure 3	Measure 4	Measure 5	Measure 6	Measure 7	Measure 8	Measure 9	Measure 10	Average	Standard Deviation
15	1	10,07	10,23	13,07	10,52	13,19	11,91	11,37	8,17	10,72	10,71	11,00	1,41
10	2	10,43	10,30	10,03	9,91	9,11	8,85	8,72	12,94	10,05	10,25	10,06	1,13
2	3	6,99	8,61	12,55	9,76	10,32	9,25	10,96	11,38	7,79	10,07	9,77	1,59
11	4	14,53	14,74	15,55	11,78	16,89	14,93	14,54	15,55	12,77	12,41	14,37	1,51
7	5	11,00	12,06	11,92	13,11	9,25	8,52	12,84	12,18	10,35	11,54	11,28	1,43
16	6	12,82	11,66	10,48	8,77	11,14	10,37	11,79	11,66	11,27	8,56	10,85	1,27
14	7	20,02	22,73	17,09	24,19	23,30	17,28	25,68	20,54	19,13	19,75	20,97	2,75
5	8	16,70	10,30	9,33	16,70	16,32	14,95	11,26	13,99	14,95	11,27	13,58	2,66
3	9	12,71	10,35	7,74	7,73	10,23	14,07	10,09	8,79	11,27	13,62	10,66	2,15
23	10	16,20	12,04	14,01	18,29	16,41	17,17	12,49	14,41	15,87	15,20	15,21	1,89
19	11	12,69	18,35	16,23	16,00	15,80	18,26	15,68	15,89	16,15	15,00	16,00	1,51
20	12	11,53	11,87	8,49	9,26	11,58	9,65	13,41	9,49	8,63	9,11	10,30	1,58
17	13	9,11	11,88	11,85	9,26	9,89	15,51	10,81	9,78	9,50	9,65	10,72	1,86
18	14	12,75	12,49	12,89	14,71	16,92	13,40	19,64	13,40	17,82	13,28	14,73	2,38
21	15	13,03	12,62	15,61	12,37	17,97	11,45	13,68	10,80	11,99	14,44	13,39	2,03
22	16	9,49	12,13	7,94	8,76	13,14	11,97	10,41	11,96	10,54	7,68	10,40	1,80

Table A.4: Random parameter values generated for the MATLAB simulation (I).

Vbands [mm/min]	**Vtable** [mm/min]	**F** [mL/h]
8000	300	1,5
5000	500	1,5
3000	125	1
1500	500	1
3000	300	1,5
1500	750	1
5000	125	4
1500	500	1,5
5000	750	2,5
8000	300	1,5
5000	500	1,5
1500	750	2,5
5000	500	2,5
5000	300	2,5
5000	500	1,5
5000	125	1
5000	750	2,5
5000	125	4
5000	300	1
5000	500	1
1500	300	2,5
1500	125	2,5
5000	750	4
3000	500	4
3000	125	1,5
1500	750	4
8000	125	1
3000	750	1,5
5000	125	1
1500	300	2,5

Table A.5: Random parameter values generated for the MATLAB simulation (II).

Vbands [mm/min]	**Vtable** [mm/min]	**F** [mL/h]
3000	500	3
1000	500	2,3
3000	600	2,3
4000	200	1,2
2000	500	2,3
1000	600	1,2
1000	200	2,3
1000	600	3
3000	200	4
3000	600	2,3
1000	500	3
2000	500	4
2000	600	3
3000	600	3
1000	200	1,2
2000	200	4
3000	600	4
2000	500	4
1000	600	4
2000	100	2,3
4000	200	3
4000	200	1,2
1000	200	1,2
2000	500	4
4000	100	2,3
2000	600	4
4000	200	3
1000	200	1,2
3000	600	3
4000	100	2,3